Chapter 2

Experimental

2.1 Introduction

This chapter will describe in some detail the design characteristics and construction of the apparatus used for vibrationally mediated photodissociation of small molecules and weakly bound molecular complexes. The experiment has been evolving continually over the course of six years, it is useful, therefore, to collect in one place a comprehensive overview of the critical elements of the apparatus in the present stage of development and to review the considerations taken into account in the design stage. Each of the major subunits is discussed separately, with emphasis on the components that are unique to this apparatus and therefore not documented elsewhere. We do not include in the current chapter the experimental details specific to each of the experiments; these will be addressed in the experimental chapters that follow.

2.2 Experiment overview

The key components of the experimental apparatus are summarized in Fig. 2.1. A slit supersonic expansion (4 cm by 50 μm, 500 μs pulse duration) is used to cool the parent H_2O molecules into the lowest rotational levels allowed by nuclear spin statistics, i.e. 0_{00} (para) and 1_{01}(ortho) and to produce the H_2O containing weakly bound complexes. As a result of the slower (1/r) drop off in gas density, the slit expansion provides high concentrations of H_2O per quantum state in the interaction

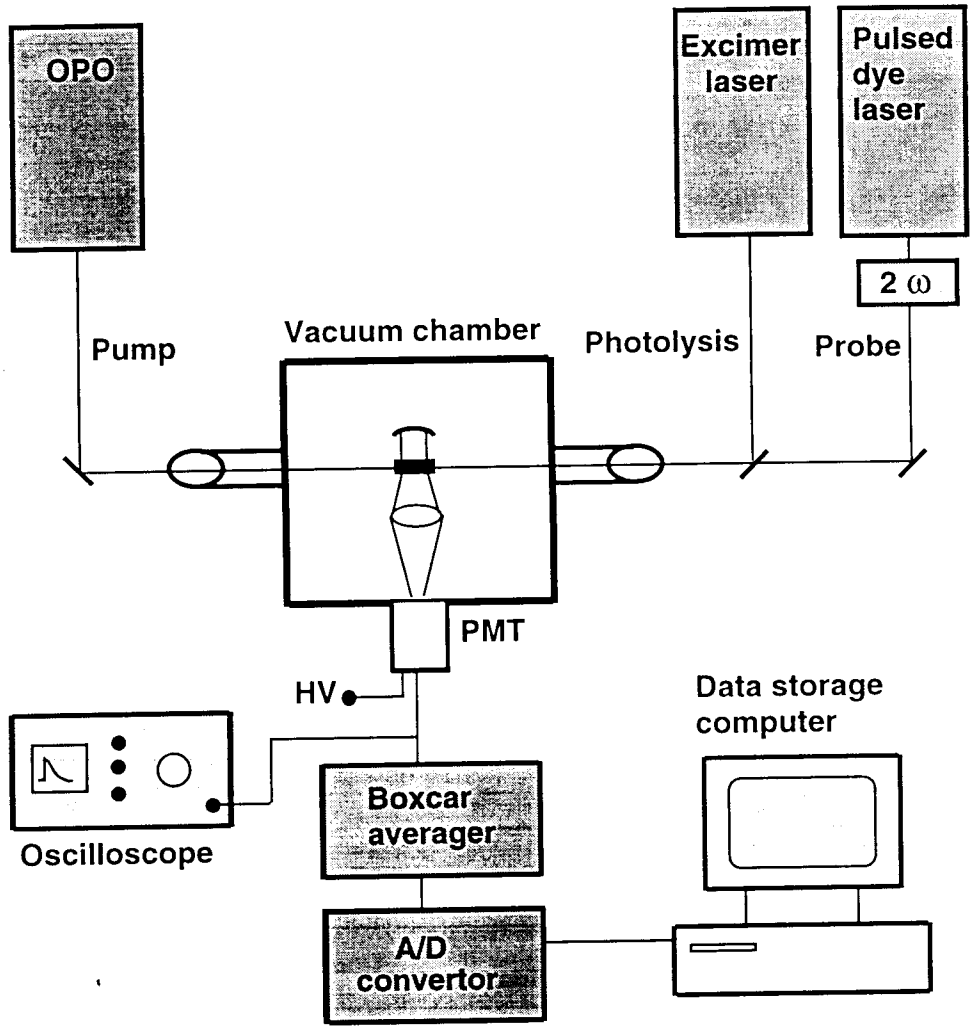

Figure 2.1: Overview of the experimental apparatus. A cold molecular beam is prepared by supersonic expansion through a pulsed slit jet to the vacuum chamber, where the molecular beam is crossed by three laser beams. First, the pump beam prepares the desired initial state of the reactants; second, the prepared states are photodissociated by the photolysis laser; third, the photoproducts are probed via LIF.

region, as well as provides a long absorption path for enhancing the signals from weak overtone vibrationaly transitions. Furthermore, the slit geometry leads to efficient collimation of velocities along the slit axis, which leads to an order of magnitude narrowing of overtone Doppler widths and thus a corresponding 10-fold enhancement of vibrationally mediated photodissociation signals for a sub-Doppler pump laser.

The jet cooled H_2O molecules or H_2O containing complexes are then efficiently pumped into specific rovibrational states in the $v_{OH} = 3$ OH stretch overtone manifold by IR pump pulses from a single mode, tunable optical parametric oscillator (OPO). This OPO is used to produce signal and idler pulses in the visible (570 nm-650 nm) and near-IR (790 nm-950 nm) spectral region, respectively. By injection seeding the resonator with a single-mode cw dye laser, a Fourier-transform-limited output of the ring OPO is achieved with a spectral width of 160 MHz (≈ 0.005 cm^{-1}).

In conjunction with output pulse energies of > 5 mJ/pulse, this OPO light source provides sufficient spectral brightness to appreciably saturate up to $\Delta v = 3$ OH stretch overtone rovibrational transitions. In combination with efficient jet cooling of parent species into the few lowest rotational levels, this permits significant optical pumping (10-20%) into a given rovibrational quantum state. For typical stagnation pressures and distances downstream from the slit nozzle, this translates into excited state H_2O monomer densities in excess of 10^{13} molecules /cm^3 and 4 x 10^{11} total molecules in the detection volume, respectively. For the water containing complexes the estimated number densities are approximately a factor of 10^3 lower compared to the H_2O monomer, due to $\approx$1% complexation efficiency and 10-fold more rotational states

thermally populated in the jet.

The vibrationally excited H_2O molecules are then selectively photodissociated by the photolysis laser pulse. This pulse is provided either by a KrF excimer laser pulse at 248 nm, or alternatively by tunable UV radiation at roughly 222 nm from frequency doubled and sum-frequency mixed output of a pulsed dye laser. Typical pulse energies of 50 mJ/ pulse and 5 mJ/pulse for the excimer and dye laser systems, respectively, are used in the experiment. At those wavelengths the vibrationally excited molecules are photodissociated preferentially, with the photolysis cross section ratio $\sigma(v_{OH} = 3) / \sigma(v_{OH} = 0) > 10^3$. The photolysis cross sections for H_2O are estimated from quantum scattering calculations described in some details in Chapter 3 to be $\sigma_{248} = 2 \times 10^{-21}$ cm^{-2} and $\sigma_{222} = 6 \times 10^{-20}$ cm^{-2}, which for typical UV pulse energies and a beam size of 1 mm^2 translates into 4×10^9 and 1×10^{10} total number of photolyzed H_2O monomer molecules in the detection volume for the 248 nm and 222 nm photolysis, respectively.

A conventional frequency doubled pulsed dye laser source provides tunable radiation in the 280 nm - 310 nm spectral region to probe the $^2\Sigma \leftarrow {}^2\Pi$ electronic transition in the OH and OD photoproducts. The LIF from a 1 mm × 1 mm × 4 cm detection volume is spatially filtered and imaged onto the PMT, using light collection assembly optics for high scattered light rejection (1:10^9) and high efficiency (about 10 %) collection along the slit dimension[1]. To obtain reliable product state distributions from the measured LIF spectra, however, considerable care must be exercised to anticipate and correct for possible LIF signal saturation. The UV probe laser is therefore operated at rather low energies typically of 2-20 μJ/pulse, a range over

which the LIF signals begin to show slight curvature with increasing power due to partial saturation of the OH electronic transition, yet still reliable enough that OH state populations can be extracted from the spectra.

2.3 The injection seeded optical parametric oscillator

In many respects the injection seeded optical parametric oscillator (OPO) is the heart of the experimental apparatus. It is the "work house" for producing the infrared radiation necessary for preparing single initial quantum states via optical pumping of the overtone transitions in the parent molecules and molecular complexes for subsequent dynamics studies. This OPO is a one-of-a-kind device, designed and built specifically for these experiments. Therefore, a more detailed description, including a brief overview of the underlying physical principles and description of the design and performance of this device, will be presented in this section.

2.3.1 Principles of operation

The optical parametric process is based on nonlinear optical properties of non-centrosymmetric crystalline materials. If two electromagnetic waves at frequencies ω_1, and ω_2 propagate through such a material, waves at the sum ($\omega_1 + \omega_2$) and difference ($\omega_1 - \omega_2$) frequencies are produced due to the nonlinear optical susceptibility of the material. Under certain conditions this effect can be exploited to create a net power transfer between the electromagnetic field components at different frequencies. Specifically, it can be shown that for the waves ω_1, ω_2 and ω_3 ($\omega_1 > \omega_2$

$> \omega_3$) propagating collinearly through the nonlinear optical crystal, two conditions must be fulfilled for the macroscopic power flow between those waves:

$$\omega_1 = \omega_2 + \omega_3 \tag{2.1}$$

$$n_1\omega_1 = n_2\omega_2 + n_3\omega_3 \tag{2.2}$$

where n_1, n_2 and n_3 are the indices of refraction at frequencies ω_1, ω_2 and ω_3, respectively.

In the framework of quantum field theory, these conditions represent requirements of energy and momentum conservation, respectively, in a process in which either two photons at frequencies ω_2 and ω_3 are annihilated to produce one photon at frequency ω_1 or vice versa, one ω_1 photon is annihilated and photons at ω_2 and ω_3 are created. [2] The constrain reflected by equation 2.2 is usually referred to as the phase matching condition, since classically it represents the requirement of constant phase relations between the the three interacting waves through the length of the crystal, which is necessary for a net energy transfer between the different frequency components. For given set of frequencies ω_1, ω_2 ,ω_3 (already fulfilling the condition $\omega_1 = \omega_2 + \omega_3$) the indices of refraction must be adjusted to fulfill the phase matching condition. Fortunately, this can be accomplished quite easily utilizing the fact that the nonlinear crystals are birefringent, and therefore, the index of refraction depends on both polarization and direction of propagation of the wave with respect to the crystal optical axis. It will be stated without further proof that for a range of frequencies (characteristic for given nonlinear material), a unique direction of wave propagation

exists in the crystal for which the phase matching condition is fulfilled. [2,3] In uniaxial crystals, this direction is determined by an angle called the phase matching angle, between the crystal optical axis and propagation direction of the beams. Therefore if a beam at frequency ω_1 passes through the nonlinear optical material at a certain direction with respect to the optical axis, net parametric gain can be created for beams at unique frequencies ω_2 and ω_3 determined by the energy conservation constraint from Eq. 2.1 and by the phase matching condition in Eq. 2.2. Those three beams are usually referred to as pump, signal and idler respectively. As an example, Fig 2.2 shows the dependence of the signal and idler frequencies for a β-Barium Borate crystal pumped at the 355 nm. The nonlinear material then acts as a laser gain medium: a weak beam at the ω_2 or ω_3 is amplified in the crystal by interaction with the strong pump field at ω_1. By placing such a gain medium in an optical oscillator resonant either at ω_2 or ω_3, a laser-like device is produced that generates coherent output at signal (ω_2) and idler (ω_3) frequencies. Such a device is called an optical parametric oscillator (OPO).

Although the potential of optical parametric oscillators as broadly tunable, all-solid-state sources of coherent radiation had long been recognized, technical limitations prevented their widespread use as high resolution devices until relatively recently. Two major advances have been i) the development of pulsed lasers with suitable single mode quality to be used as OPO pump sources, such as now available with narrow band, injection seeded Nd:YAG lasers, and ii) improved nonlinear optical materials such as β-Barium Borate (BBO)[4-8] and Lithium Borate (LBO)[5,9] with optical properties and high damage thresholds suitable for efficient OPO operation.

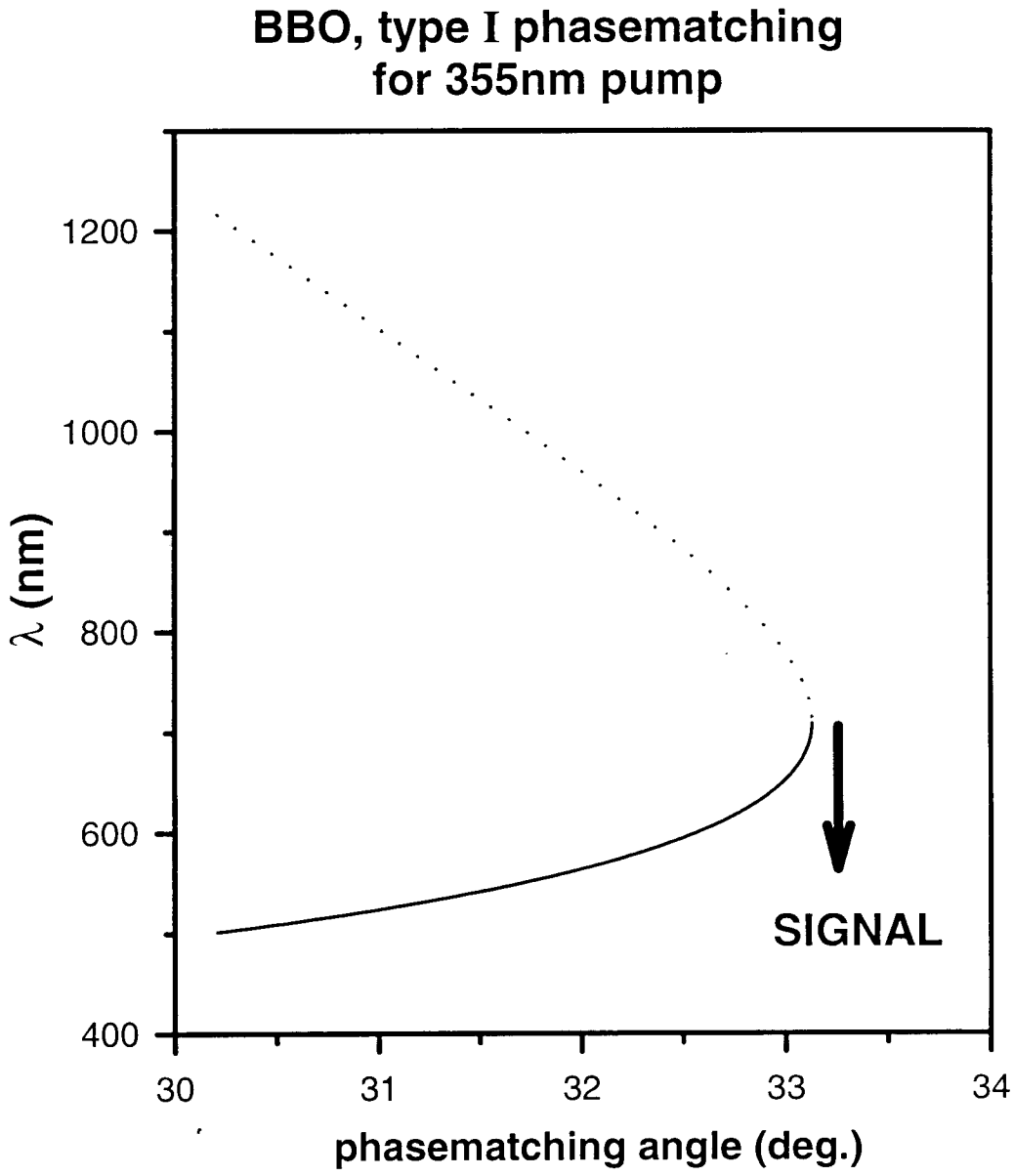

Figure 2.2: Wavelength of the signal and idler waves as a function of the phase matching angle for β-Barium Borate crystal pumped at 355 nm.

In the absence of any frequency narrowing scheme, the linewidth of an OPO output is limited by the angular phase matching condition in the nonlinear medium, which can be unacceptably broad ($\Delta\nu \geq 1$ cm^{-1}) for many spectroscopic applications. This is especially true for multiple resonance spectroscopies, where spectral brightness (i.e., pulse energy per unit frequency bandwidth) is the limiting quantity, rather than simply pulse energy. Additionally, the unnarrowed OPO line width is strongly wavelength dependent, increasing considerably as the degeneracy point ($\omega_{signal} = \omega_{idler} = 1/2\ \omega_{pump}$) frequency is approached. A number of narrowing techniques have been proposed and implemented to reduce OPO line widths closer to the Fourier transform limit. If only modest resolution is needed, one of the cavity mirrors can be replaced by an optical grating in Littrow configuration,[7,10-12] with higher resolution schemes requiring several frequency selective elements to tune synchronously.[13,14] In the state of the art OPO designs of this latter kind, single mode operation has been achieved over a broad tuning range, but at the cost of decreased efficiency and considerable complexity of such devices.

A powerful alternative method for frequency narrowing is via OPO injection-seeding with narrow-band radiation from an external laser source. In an unseeded OPO, all the cavity modes initially build up in power at a comparable exponential rate, typically resulting in multimode oscillation. By way of contrast, if the cavity already has circulating power due to injection seeding, the power in the seeded longitudinal mode builds up rapidly during the pump pulse compared to the other cavity modes, which then depletes the parametric gain before the other modes can

reach threshold. Single mode operation of the OPO can thus be achieved in pulsed operation, with the output frequency locked onto the injection seed source.

2.3.2 OPO Cavity Design

The overall layout of the optical parametric oscillator is schematically shown in Fig. 2.3. The setup consists of i) a planar four-mirror OPO ring cavity, ii) a single mode (pulsed) pump laser and iii) a single mode (cw) injection seed laser. If one neglects weak mode pulling effects to be discussed later, the signal OPO output oscillates at the same frequency as the seed laser, while the idler frequency is dictated by energy conservation ($\omega_{idler} = \omega_{pump} - \omega_{signal}$). For 355 nm pump radiation and injection seeding with a cw R6G dye laser, the idler provides access to the 800-1000 nm region, which overlaps conveniently with the $\Delta v = 3$ overtone bands in the OH, CH and NH stretch manifolds.

Details of the OPO resonator design are shown in the Fig. 2.4. The parametric gain of the OPO cavity relies on a pair of 10 mm BBO crystals with 5 x 6.5 mm^2 entrance faces. The angle between the crystal optical axes and the entrance face normal is 28.5°, i.e., the crystals are cut for type I phase matching, with the signal and idler beams polarized along the 5 mm edge. Both BBO crystals are cut from the same boule to ensure matching optical properties, with input and exit surfaces anti-reflection coated at the signal wavelength to avoid intracavity reflection loses in the OPO resonator. The two crystals are mounted in precision rotational stages in the walkoff compensation arrangement described by Bosenberg[15], see lower panel in Fig. 2.4.

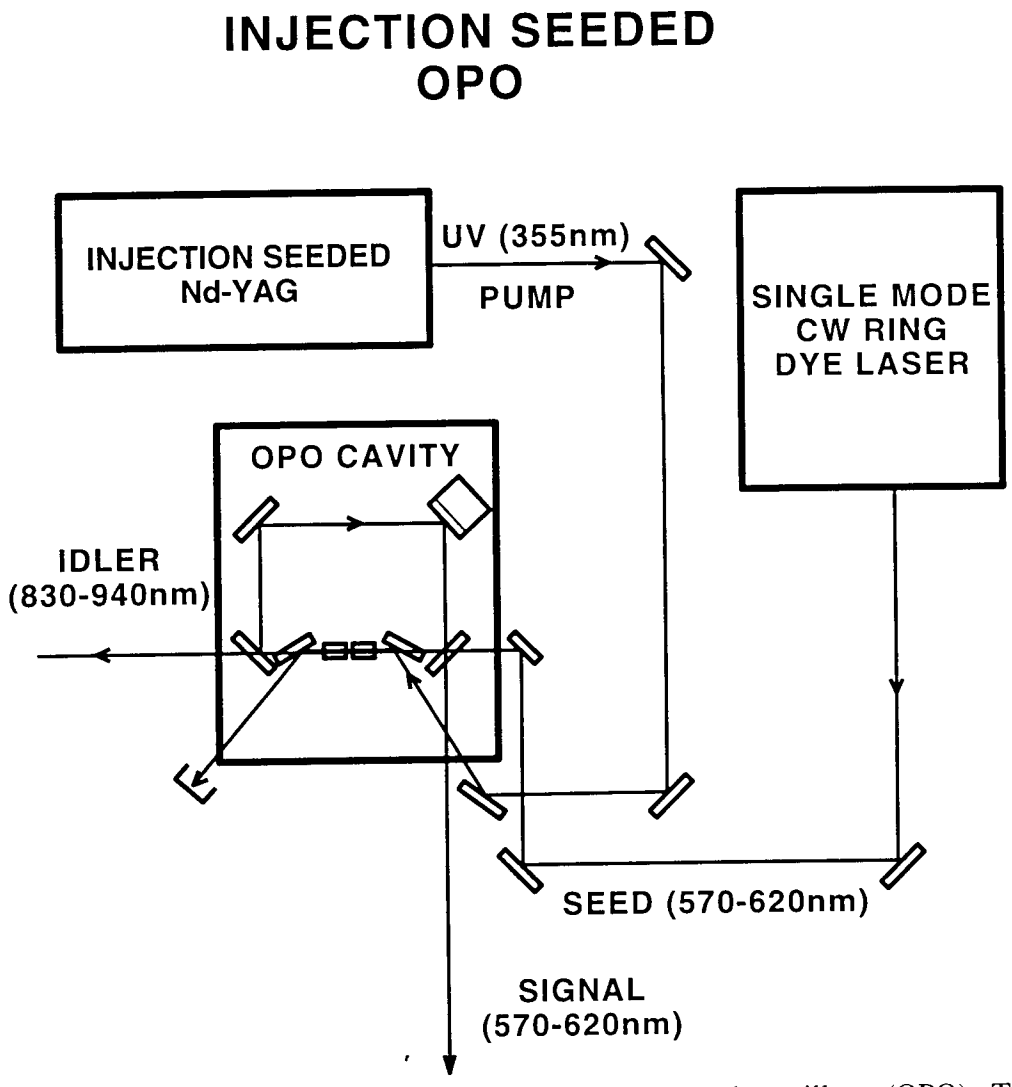

Figure 2.3: Schematic of the injection seeded optical parametric oscillator (OPO). The OPO cavity is pumped by the third harmonic of a pulsed Nd:YAG laser at 355 nm and injection seeded by a tunable cw dye laser. The signal output of the OPO coincides in frequency with the seed dye laser, while the idler accesses the near IR region.

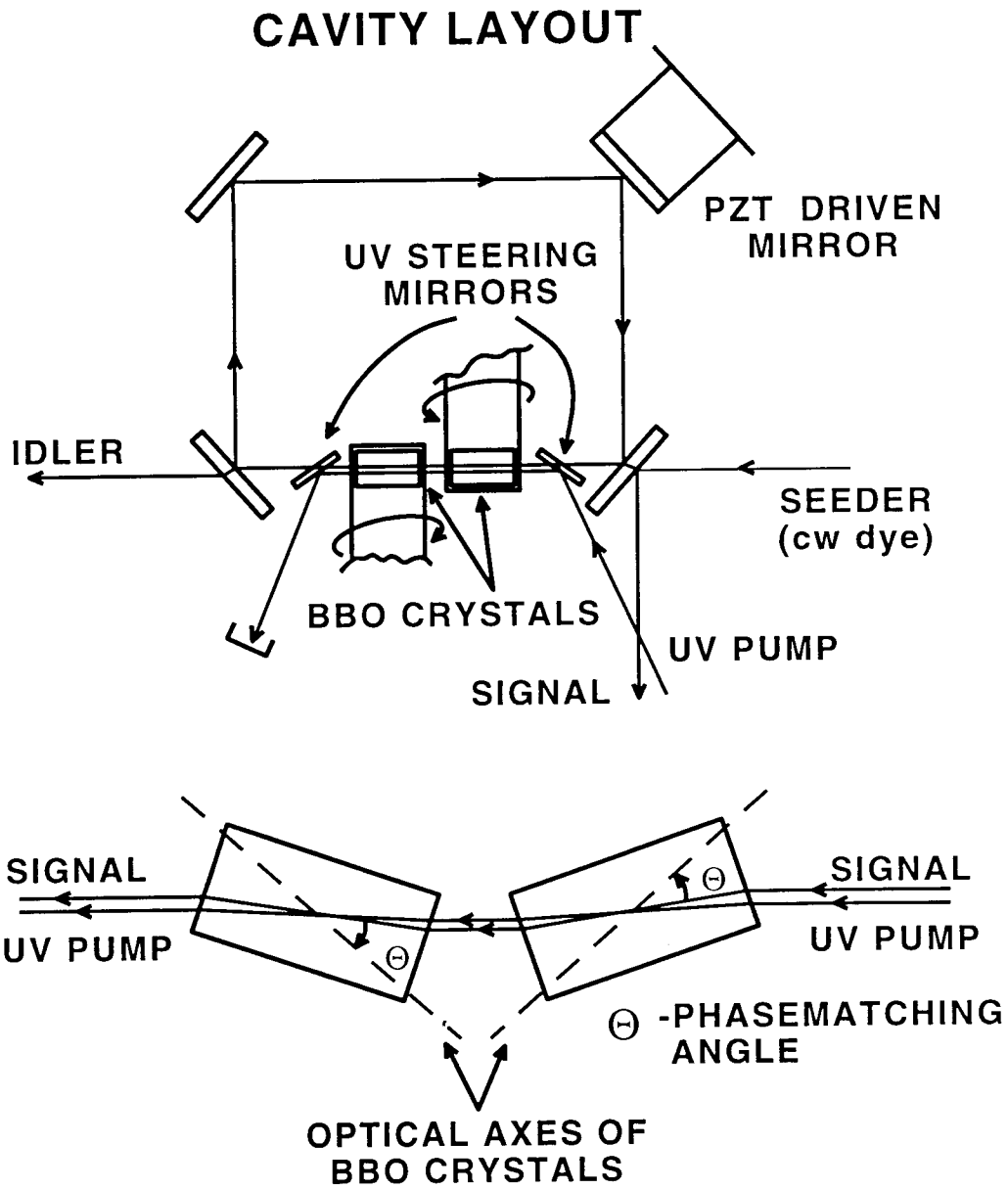

Figure 2.4: Schematic of the OPO cavity. The optical resonator is formed by a four flat mirror ring cavity with two BBO crystals in a walk-off compensating arrangement. The PZT mounted mirror permits servo loop locking of the resonator to the seed frequency. Pump radiation is introduced into the OPO ring via a pair of UV Brewster steering mirrors.

Four flat mirrors define the OPO ring cavity, which by choice of mirror reflectivities and servo loop feedback is singly resonant with the seed frequency. The important advantages of the ring cavity design are ease of alignment, lack of spatial hole burning in the gain medium, unidirectional output, and optical isolation of the OPO pulse from back reflection into the seed dye laser. The free spectral range (FSR) of the resonator is 1.35 GHz (0.045 cm^{-1}), which corresponds to a round trip time of 0.73 ns and thus roughly 10 optical round trips during the 7 ns pump pulse. For servo loop locking the cavity mode onto the seed laser, one of the cavity mirrors is mounted on a piezoelectric (PZT) transducer; this allows tuning of the OPO cavity over two full free spectral ranges with negligible displacement of the beam over any continuous single mode scan. The input/output coupler is 80% reflective at the signal wavelength, while the other cavity mirrors are highly reflective (> 99%). This output coupler reflectivity dominates the round trip loss in the cavity and yields a resonator finesse of 8±1. This finesse is also close to the number of cavity round trips during the pump pulse, which optimizes OPO conversion from pump to signal/idler. All four mirrors have high transmission in the 800 - 1,000 nm idler region to prevent doubly resonant behavior and possible mode competition between signal and idler OPO output. Furthermore, although the ring cavity mode structure itself can support oscillation in both clockwise and counterclockwise directions, the OPO parametric gain is exclusively in the direction of the pump pulse/seed laser. Consequently, the entire idler output can be efficiently extracted at the first mirror "downstream" of the BBO crystal pair.

The OPO is pumped by the third harmonic of a Fourier transform limited, pulsed

Nd:YAG laser at 355 nm. The oscillator of the pump laser is injection seeded by a cw single mode YAG laser in order to obtain single mode pulsed operation and a smooth temporal time profile. Maximum available energy from the pump is 200 mJ in 7 ns pulses, yet to prevent exceeding the damage limits of the cavity mirrors, only a fraction of the full pulse energy (50 - 100 mJ/pulse) is typically utilized. The pump beam size at the Nd:YAG laser output is 7 mm FWHM and slightly divergent. The beam is collimated with a Galilean telescope (2:1 reduction ratio) to match approximately the size of the BBO crystals in the OPO resonator. At the output of the Nd:YAG pump laser, the transverse mode quality is better than 80% TEM_{00}. In order to achieve the far field limit and smooth any potential 'hot spots' in the spatial profile, the pump beam is propagated for 4 meters before it enters the OPO resonator. The pump radiation is coupled into the crystals via two intracavity steering mirrors, coated for high reflectivity at 355 nm and high transmissivity at signal and idler wavelengths. The pump coupling mirrors are placed at Brewster's angle with respect to the signal beam to reduce intracavity reflection losses as well as to prevent the high intensity pump radiation from exceeding the damage threshold for the broad band cavity mirrors. Furthermore, these mirrors serve as polarization selective elements in the OPO resonator, which prove useful in locking the cw dye laser to the cavity via polarization servo loop control, (see section 2.3.3 below).

The OPO cavity is injection seeded by an Ar^+ pumped single mode cw ring dye laser. Short-term frequency stability ($\leq$ 1 MHz) of the injection seed is achieved by locking the dye laser to a fringe of a pressure and temperature stabilized reference Fabry-Perot interferometer.[16] Specifically, drift of the seed ring dye laser and OPO

output is demonstrated to be less than ± 2 MHz over several hours. The seed laser can be single mode scanned under computer control over a range of up to 2 cm^{-1}, with arbitrarily longer frequency ranges covered by concatenation of overlapping scans. Due to the highly nonlinear nature of the OPO parametric conversion process, typical power outputs from the cw dye laser (greater than 100 mW) represent much higher injection seed levels than necessary; tests with seed power levels down to a few mW indicate no significant drop off in the OPO pulse output. This is qualitatively consistent with other OPO systems such as reported by Lehmann,[17] Bosenberg,[18] or Milton,[19] where input power levels even at the several mW level proved adequate for achieving single mode output. However, this excess of injection seed power is used to good advantage by expanding the ring laser spot size before it enters the OPO resonator to overfill the 355 nm pump beam.

2.3.3 OPO Cavity Locking

For efficient injection seeding of the OPO, the longitudinal mode of the resonator must be matched with the frequency of the seed radiation. To achieve this, the OPO resonator is locked to the seed frequency by servo loop control of the cavity length with the internal PZT mounted mirror. The servo loop scheme is based on polarization locking methods first introduced by Hänsch and Couillaud[20] (see Fig. 2.5), which rely on the differential phase shift between s-and p-polarized modes of the ring resonator. Specifically, the linearly polarized seed laser is rotated by 10^{o} away from horizontal (p-polarization) to generate a weak s-polarized component and injected into the OPO ring. Due to lossy Brewster elements and a lower finesse, the

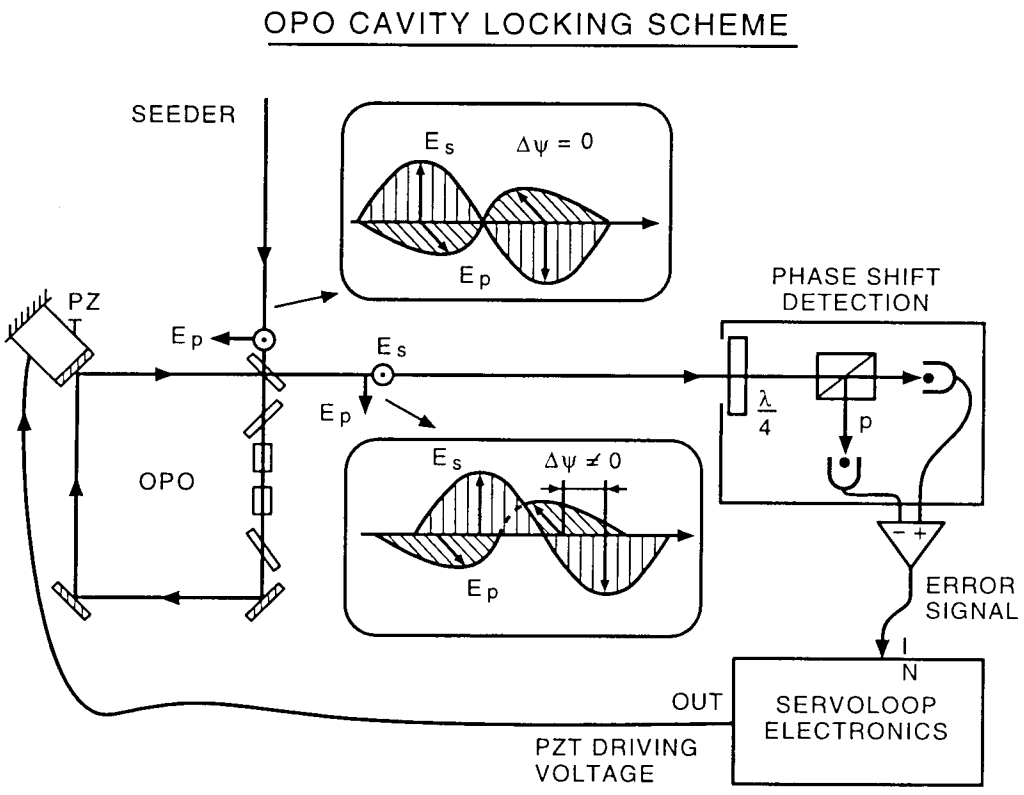

Figure 2.5: Polarization locking scheme adapted from ref 22. The optical phase shift between two perpendicularly polarized light components induced by the OPO resonator is detected by subsequent polarization analysis with a λ/4 plate, a linear polarizer and two photodiodes. The resulting error signal locks the OPO resonator onto the scanning seed dye laser by servoloop feedback to the PZT mounted cavity mirror.

s-polarized component is essentially reflected from the input mirror with negligible phase shift due to the time spent in the cavity. The reflected light of p-polarization, on the other hand, suffers a rapidly changing phase which passes through zero (modulo 2π) as the laser is tuned through the cavity resonance. Thus, recombination of the s and phase shifted p-components results in an elliptical polarization for the light reflected from the input coupler, where the magnitude and sign of the two polarization components contain resonance information on the cavity. This information is extracted with a quarter wave plate plus polarization beam splitter (see Fig. 2.5), with the two polarization signals incident onto a pair of balanced photodiodes. Subtraction of these two photodiode outputs results in a steeply varying discriminator signal suitable for servo loop locking onto the resonance cavity condition. Such a method has the significant advantage of being "dither-free", i.e., requiring no modulation of the cavity nor subsequent phase sensitive detection of the modulated signal. As described below, this permits much simpler servo electronics and faster lock recapture after the OPO amplified seed pulse.

The error signal from the balanced photodiodes is processed by analog servo loop electronics (with both integral and proportional gain) to generate an amplified output voltage on the intracavity PZT mounted mirror. The OPO resonator is thereby locked to the zero crossing of the error signal, corresponding to zero optical phase shift in the resonator. The frequency response of the servo loop is limited by a LC filter to roll off at 5 kHz, with a unity gain frequency at 8 kHz. This bandwidth restriction is chosen for two reasons. First, mechanical resonances of the piezo driver and mirror assembly occur at approximately 10 kHz, which can result in additional phase shift

instabilities. More importantly, however, the small fraction of the resulting OPO signal radiation which leaks through the input coupler exceeds the seed power level by many orders of magnitude, which saturates the balanced photodiodes and drives the error signal out of limits during the pump pulse. By limiting the electronic bandwidth to 5 kHz, one prevents the servo loop from responding to these false error signal disturbances during the OPO pulse; the cavity mirrors are effectively "frozen" in place so that the cavity stays in resonance with the seed frequency. Consequently, the servo loop rapidly reacquires the lock within 1 msec after the OPO pulse, i.e., on a time scale short compared to the pump laser repetition rate (t_{rep} = 1/10 Hz = 100 msec).

An important feature of the current OPO design is the ability to scan the output continuously in frequency, which is achieved by scanning the frequency of the single mode seed laser. This in turn requires the OPO cavity to remain actively locked to the seed laser throughout a 2 cm^{-1} scan. The OPO cavity scan range, on the other hand, is restricted by translation of the PZT mounted mirror; with a 2.54 cm long PZT element and < 1 kV voltage excursions, this is currently limited to two FSR, i.e., approximately 2.7 GHz. The PZT voltage must therefore be shifted down/up by the equivalent of one FSR whenever preset high/low voltage limits on the PZT are reached. To achieve this, the PZT servo loop i) follows the cavity mode to the end of its voltage range and ii) automatically reacquires the lock on the next cavity mode to continue the scan. The time scale on which the servo loop breaks and reacquires the lock on the next mode is also sufficiently short ($\leq$ 10 msec) compared to the OPO repetition rate that no output pulses are influenced. The robustness of this scheme can

be tested by monitoring the error signal (in units of MHz) while scanning the single mode dye laser with and without the OPO cavity lock. As shown in Fig. 2.6, the error signal in the absence of the lock executes periodic excursions every 1.35 GHz, corresponding to the FSR of the OPO cavity. With the cavity lock activated (Fig. 2.6) on the steep discriminator slope near $\Delta\nu = 0$, the error signal is actively driven to zero, with a rms frequency deviation of $\leq$ 10 MHz. This is within 6% of the cavity fringe width, ensuring that the injection seed laser is fully "preresonating" the OPO prior to the arrival of the 355 nm pump pulse.

2.3.4 Single Mode OPO Spectral Resolution

The most important effect of cw injection seeding the OPO resonator is the dramatic narrowing of the output frequency line width, from an unseeded line width of 10 cm^{-1} to single longitudinal mode operation ($\Delta\nu = 0.005$ cm^{-1}) with seeding. This single mode operation is explicitly demonstrated in Fig. 2.7, in which the line width of the pulsed OPO output has been measured in transmission using an independent, high finesse (> 200) Fabry-Perot interferometer. The measured line width has a full width at half maximum (FWHM) of $\Delta\nu_{FWHM} = 160(20)$ MHz, with a line shape that is intermediate between Lorentzian and Gaussian. The finesse limited line width from the Fabry-Perot (2 GHz FSR) is $\leq$ 10 MHz (as measured with the cw seed laser source), and therefore the observed transmission profiles can be entirely ascribed to OPO line width contributions. It is worth noting that these measured line widths reflect several hundred OPO pulses and so represent a rigorously conservative upper limit to *single* pulse spectral resolution.

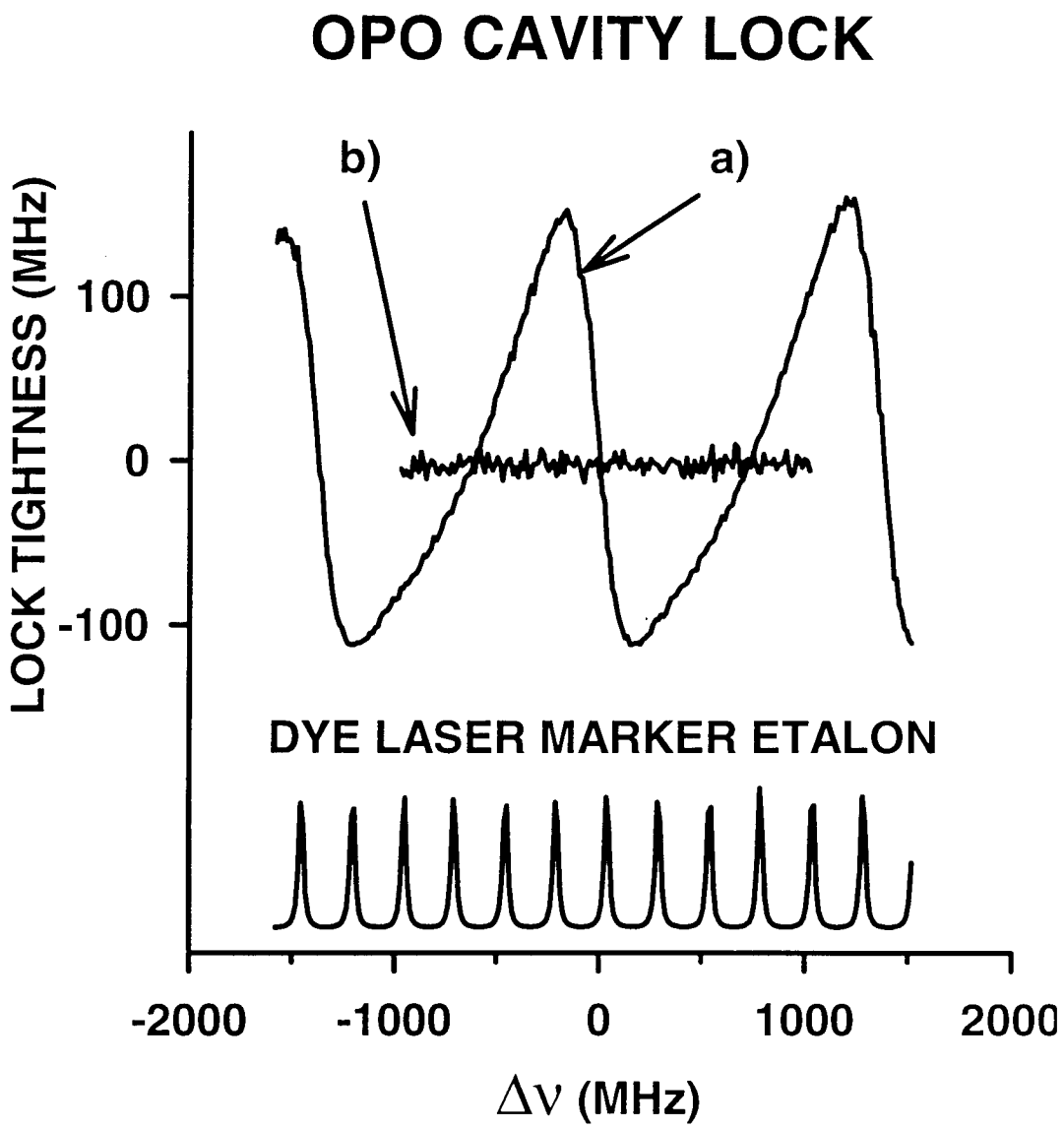

Figure 2.6: OPO cavity tracking. a) With the feedback servo disabled, the polarization phase shift derived error signal varies as the dye laser is scanned. The rapid downward going signal corresponds to tuning through a cavity resonance with the seed laser. b) With the servo enabled, the error signal is driven to zero by PZT control of the cavity length, thus actively tracking the injection seed frequency throughout a single mode scan. The width of the error signal translates into a rms frequency noise on the cavity of $\leq$ 10 MHz.

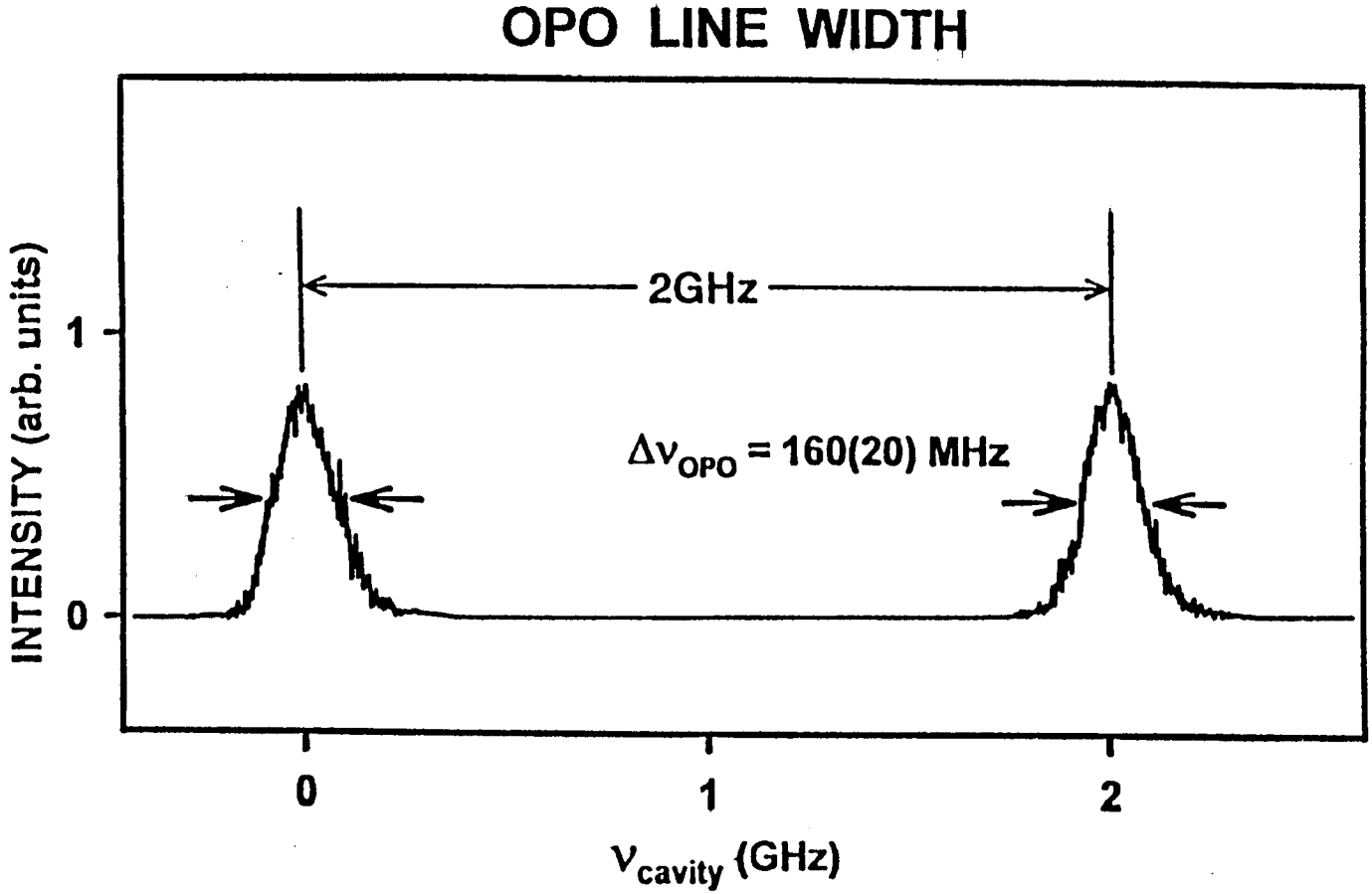

Figure 2.7: OPO line width. The line width of the OPO output is measured with a high finesse (>200) Fabry-Perot etalon (FSR = 2 GHz). The measured spectral line width of 160(20) MHz is essentially at the Fourier transform limit for a 3.5 nsec long output pulse.

The lower limit of line width for a pulsed light source is related to the Fourier transform of the temporal profile, with $\Delta\nu_{FWHM} \times t_{FWHM} = 0.44$ predicted for Gaussian shapes[21]. In the time domain, the OPO output pulses exhibit a $\Delta t_{FWHM} = 3.5(5)$ ns, with a rapidly rising edge followed asymmetrically by a somewhat slower decay. If one approximates this Δt_{FWHM} as a purely Gaussian time profile, then the Fourier transform relation would predict $\Delta\nu_{FWHM} = 130(20)$ MHz, which is quite close to but slightly smaller than the 160(20) MHz line widths observed experimentally. This is also consistent with the asymmetries in the temporal profile, which would broaden the 130(20) MHz prediction into better agreement with experiment. In summary, these combined frequency and time domain measurements demonstrate that the OPO output pulses are essentially Fourier transform limited, even averaged over many hundreds of pulses.

2.3.5 Tunability and injection seeding efficiency

Broad band tunability is one of the key advantages of optical parametric oscillation methods. With BBO crystals pumped by a 355 nm laser, the idler radiation can be tuned from the degeneracy point at 710 nm to the BBO absorption edge at 2200 nm, corresponding to a signal frequency from 710 nm to 420 nm. Since the dielectric mirrors used in the resonator provide reflectivity in a far narrower spectral window, several sets of cavity mirrors are necessary to achieve the complete tuning range of the OPO. For the applications in this paper, only one set of mirrors is used (see Fig 2.8), which limits the current OPO tuning range somewhat arbitrarily to 550 - 680 nm

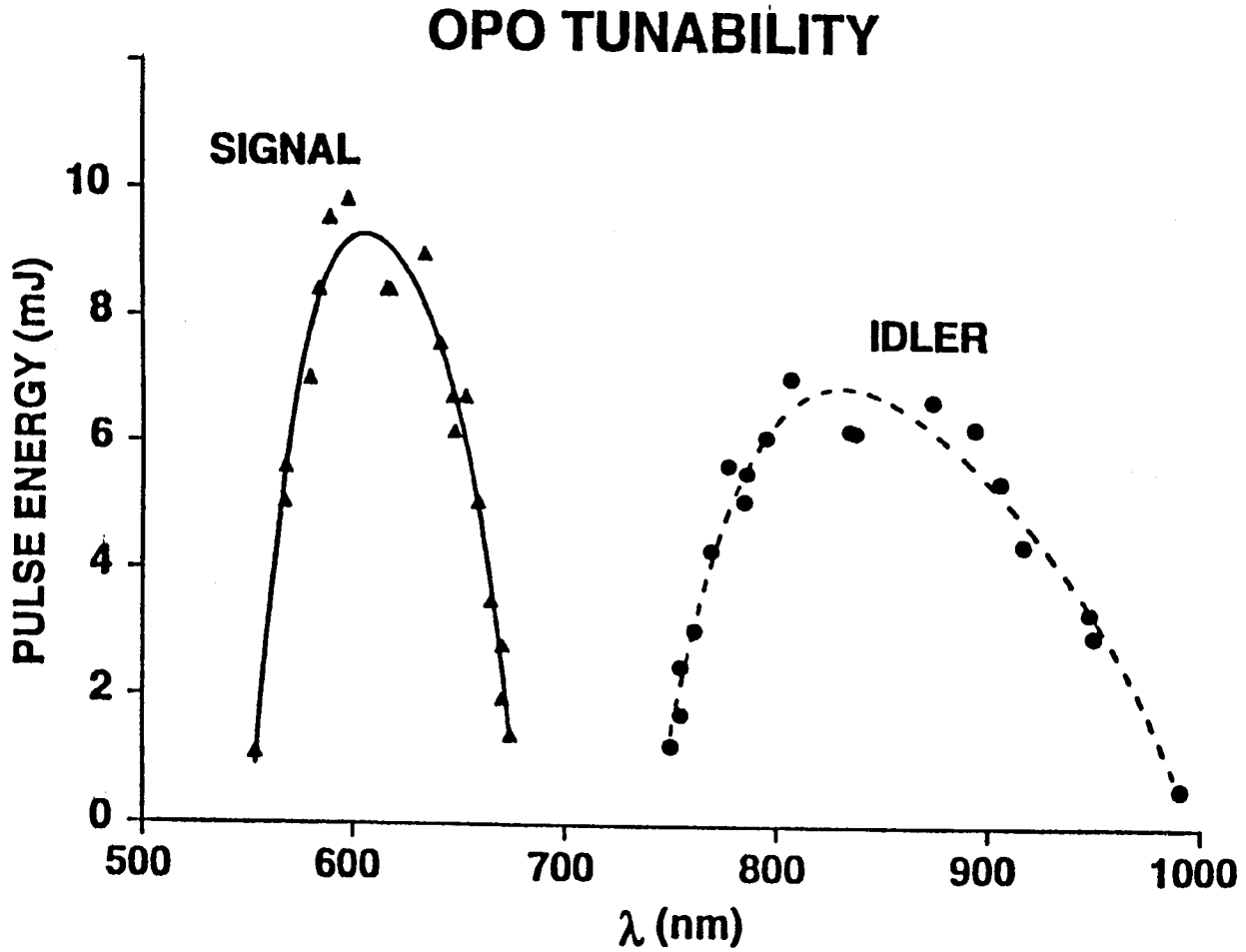

Figure 2.8: OPO tunability and typical pulse energies for the signal and idler with a single set of cavity mirrors. The tuning range is limited entirely by the reflectivity of the mirrors.

(signal) and 750 - 950 nm (idler). However, this idler range conveniently covers the $v_{OH} = 3 \leftarrow 0$ and $v_{CH} = 3 \leftarrow 0$ overtone regions in simple species such as H_2O and HCCH, as well as in molecular clusters containing these chromophores.

Injection seeding also reduces the build up time in the OPO resonator compared to unseeded operation. Since the pump pulse is relatively short (τ_{pump} = 7 nsec) and corresponds to only 10 round trips of the cavity, this effect dramatically increases the OPO conversion efficiency, especially when operated near threshold (25 mJ/pulse, 355nm pump, 3 mm beam diameter). Even at pump powers twice the threshold value, however, one observes more than a factor of two enhancement of the OPO output pulse energy for seeded vs. unseeded operation. At 355 nm, the OPO is pumped with < 100 mJ/pulse, limited currently by the optical damage threshold of the cavity mirrors. At these maximum pump energies, OPO output energies of 16 mJ/pulse for signal and 12 mJ/pulse for idler beams can be achieved, corresponding to a total conversion efficiency of 28%.

Of particular relevance to high resolution spectroscopic applications is that injection seeding permits single mode scanning of the OPO output without additional frequency selective elements in the cavity. Within the approximate 10 cm^{-1} parametric gain window of the BBO crystal, the OPO frequency output tracks the seed laser input, which in turn can be scanned with single mode resolution. Furthermore, since the typical single mode tuning range of the seed dye laser (2 cm^{-1}) is considerably narrower than this parametric gain window, it is unnecessary to adjust the BBO crystals synchronously with the dye laser for any one scan. Slight cavity angular adjustments are necessary only every 4-6 cm^{-1}, with concatenation of

arbitrarily long single mode OPO scans made possible via optical transfer cavity (TC) methods briefly summarized below.

2.3.6 Frequency Stability and Calibration

To take advantage of single mode OPO performance in high resolution applications, frequency stability and calibration are essential. Since the signal and idler frequencies are controlled by the frequencies of seed and pump radiation, this requires that both seed and pump lasers be frequency stabilized using an absolute optical transfer cavity (TC), see Fig. 2.9. As described in detail elsewhere,[16,22] an open confocal Fabry-Perot transfer cavity (TC) is locked onto the output of a He-Ne laser operating in two adjacent longitudinal modes, which is in turn locked to the center of the He-Ne gain profile by polarization stabilization methods. The TC mirrors are specially coated to provide adequate finesse (roughly 20) for both 1.064 nm (cw Nd:YAG laser) and visible (dye laser) spectral regions. The 355 nm pump laser frequency output is thereby frequency stabilized by locking the cw Nd:YAG laser that injection seeds the main Nd:YAG oscillator. Specifically, a small split off of the cw Nd:YAG laser is monitored in transmission through the TC and locked onto a cavity resonance by electronic feedback control of the Nd:YAG seed laser temperature. Drift in the 355 nm pump frequency can be reduced to 2 MHz levels, limited predominantly by pressure dependent index of refraction differences between the He-Ne and 1.06 nm laser frequencies. Similarly, the frequency of the cw seed dye laser can be locked on another transmission fringe of the same TC. Although this could also be done with analog servo loop electronics, this is most readily

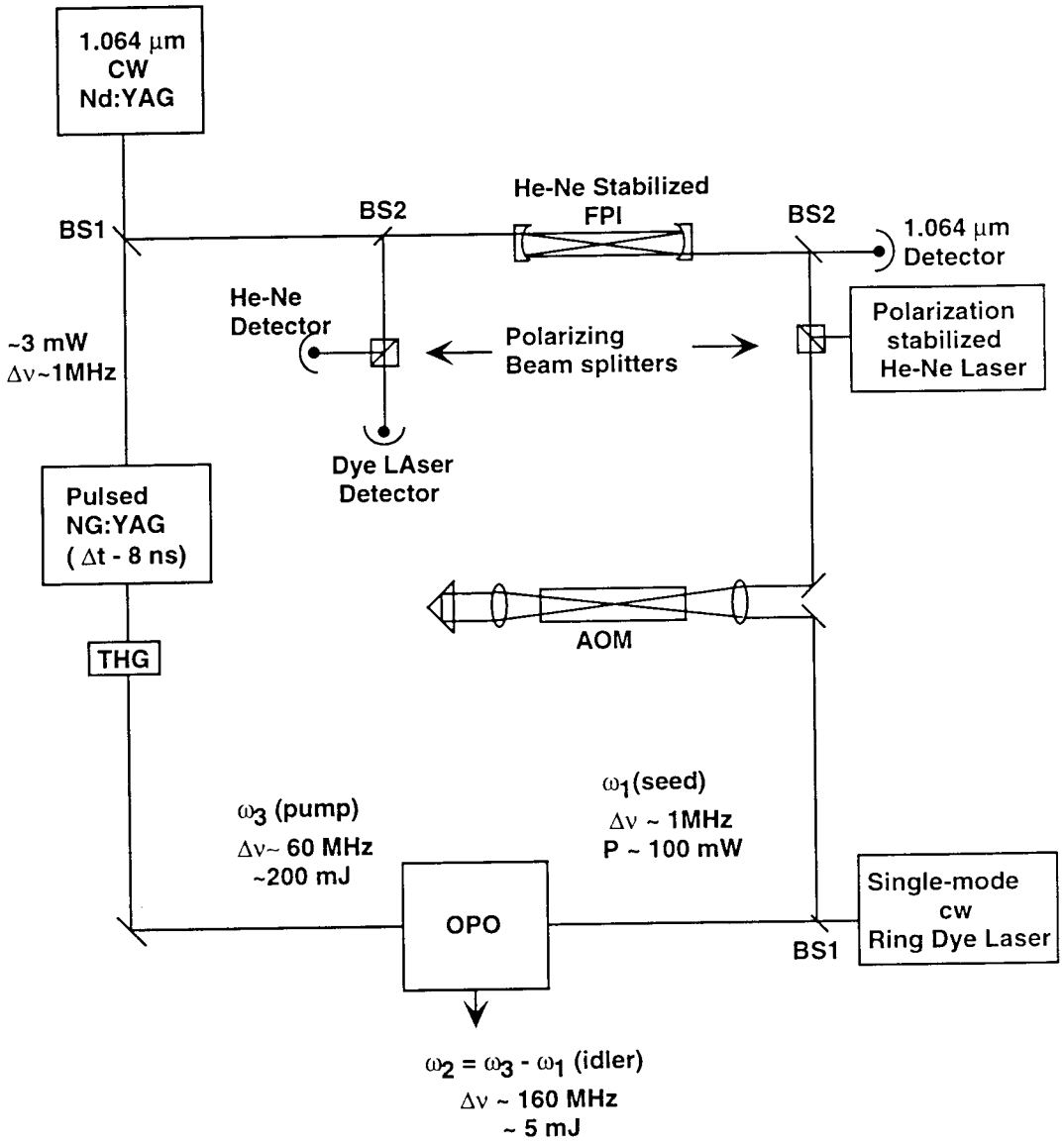

Figure 2.9: Frequency stabilization scheme for the injection seeded OPO.

accomplished with a computer controlled 16 bit D/A transducer which scans the laser in < 1 MHz steps. In this fashion, the laser can be tuned to the top of a TC transmission fringe and stabilized with digital servo loop control.

However, this method only permits the seed dye laser to be locked to the discrete, uniformly spaced (FSR = 250 MHz) transmission fringes of the TC. To provide both continuous and frequency stabilized tuning capability, a small portion of the dye laser beam is doubly passed through an acousto-optic modulator (AOM) prior to locking onto the TC. This generates frequency shifted "side band" replicas of the dye laser, with 2,4, ... quanta of the 60-140 MHz AOM added or subtracted from the dye laser frequency. The frequency of the sideband can then be tuned by adjusting a radio frequency (RF) source that drives the AOM, so long as the tuning range exceeds one half of the free spectral range of the TC. Thus, by "frequency offset locking" one of the side bands to the TC, the dye laser can be tuned to an arbitrary frequency, yet with a long term stability still equivalent to that of the reference cavity fringe.

Although both seed and pump lasers are stabilized absolutely, recent studies indicate that the high resolution OPO output can still be shifted with respect to the seed frequency due to nonlinear "mode pulling" effects in the OPO cavity.[17] Indeed, shifts between the seed and signal laser frequencies of up to 250 MHz have been reported,[23] which if not constant over time, could translate into OPO frequency drifts of this magnitude. The magnitude of the mode pulling effects have been explicitly measured in our OPO cavity design[16] by measurement of the shift between the pulsed OPO signal and cw seed laser transmission fringes in a high finesse (>200) Fabry-Perot interferometer. Specifically, the OPO output signal is consistently blue shifted

with respect to the seed by approximately 100 MHz. The magnitude of this shift depends on pump and seed beam alignment/power in the OPO resonator, but for a given set of operating conditions this shift is relatively constant (< 10 MHz) on the time scale of several hours. It is worth noting that this mode pulling still represents only a small fraction of the 160 MHz homogeneous OPO line width. With both pump and seed stabilized to < 2 MHz, however, these small residual mode pulling effects currently represent the limiting contribution to our long-term OPO frequency drifts.

Due to PZT creep and mechanical drift, long-term measurements of frequency stability at this level are notoriously difficult to obtain reliably with high finesse cavities. Thus, independent *molecular* measurements of the absolute frequency stability of the signal/idler have been performed, based on IR/UV vibrationally mediated photodissociation methods first developed by Crim and coworkers[24,25] and Andresen and coworkers.[26] Specifically, H_2O molecules are cooled to their lowest nuclear spin states in a slit supersonic expansion, which by virtue of collisional quenching of translational degrees of freedom yields sub-Doppler velocity distributions when probed along the slit dimension. At the 10 K temperatures measured in the slit jet, this corresponds to linewidths of 170(10) MHz in the second overtone band region, which is six fold narrower than room temperature Doppler widths. The OPO idler is used to excite the $v_{OH} = 3$ second overtone ($|03\rangle^- \leftarrow |00\rangle^+$) upper state, which is then photolyzed by 248 nm excimer light to form H (^2S) + OH ($X^2\Pi$). Since 248 nm excimer photolysis of the vibrational ground state occurs via Franck Condon factors down by at least three orders of magnitude, the overtone absorption event is signalled by the appearance of OH radicals, which are detected via

conventional laser induced fluorescence (LIF) on the 308 nm A ← X band.[27]

With this double resonance method, the absolute frequency stability and linewidth of the OPO can be measured in two ways. First of all, high resolution scans over individual rotational lines [$(1_{01}) \leftarrow (0_{00})$, para H_2O and $(0_{00}) \leftarrow (1_{01})$, ortho H_2O] in the second overtone band are performed. Fits to a Gaussian line shape yield 230(15) MHz; this is in excellent agreement with predictions of 233(22) MHz based on the quadrature sum of a 170(10) MHz Doppler and 160(20) MHz OPO contributions to the line width. Secondly, the long term frequency stability is investigated by tuning the idler to the steeply changing side of a specific sub-Doppler overtone line shape. Frequency instability in the idler therefore translates into excess LIF signal intensity fluctuations, from which one can establish an upper limit of $\leq$ 10 MHz rms drift in the OPO over several hours of observation.[16]

2.4 Photolysis laser systems

2.4.1 Excimer laser

As once stated by my colleague Bill Chapman, an excimer laser is basically a huge spark plug. While it clearly is an overstatement, indeed the excimer laser is fairly simple device compared to the sophistication of the high resolution OPO described in the previous section. Excimer lasers operate in a gas mixture at high pressure (P about 3000 Torr) containing a halogen (F_2 or HCl) and an inert gas such as Ar, Xe, or Kr in typically He or Ne buffer. By electron bombardment in a discharge through this gas mixture, exited state molecule (excimer) such as ArF* are formed, which are

unstable in the ground state and therefore dissociate immediately upon emitting light. Therefore almost no ground state population is formed in this bound-dissociative transition, which results in very high gain of this type of laser scheme. The output frequency is characteristic for each of the gas mix, for experiments described in this thesis KrF emission at 248 nm is used, while for preliminary direct H_2O photodissociation experiments, ArF mix was used emitting 193 nm. In the standard arrangement with transverse discharge and low-finesse optical resonator, those lasers are convenient sources of high intensity pulsed ultraviolet radiation with low spectral and spatial coherence.[28] The basic operational parameters of the Lextra 50 excimer laser used in our laboratory are summarized in Table 2.1. Under typical experimental conditions we use 50 mJ/pulse of the excimer energy with the repetition rate 10 Hz. This laser is fairly close to a turn-key device in typical day-to-day operation. The most frequent routine maintenance includes gas mix change, which is required after typically 10 hours of operation for the ArF mix, and 30 days for the KrF mix, respectively.

The rectangular output beam with different divergence in the vertical and horizontal directions is difficult to bring to a tight focus with ordinary spherical optics. Also the beam size at the output of the laser is too big to fit conveniently to standard size (ϕ = 1") optics. Therefore the horizontal dimension of the beam is reduced with a 3:1 compressing telescope formed by a pair of quartz cylindrical lenses. The beam after the telescope is close to square in shape with almost equal divergence in vertical and horizontal planes and is readily focused to a well defined spot in the center of interaction region by a single f = 1000 mm spherical lens.

Table 2.1: Excimer laser operational parameters specified by manufacturer [29]

Laser medium	Ar-F	Kr-F
Wavelength (nm)	193	248
Max. pulse energy (mJ/pulse)	200	300
Max. repetition rate (Hz)	30	30
Pulse-to-pulse energy stability (%)	3	1.8
Beam dimensions w x h (mm)	~8 x 23	~8 x 23
Beam divergence w x h (mrad)	1 x 3	1 x 3
Time jitter (ns)	2	2

2.4.2 Pulsed dye laser with nonlinear wave length extension

The excimer laser provides only a fixed wavelength output defined by the gas mix. In some cases it is important to have the ability to tune the photolysis wavelength. For that purpose we use a tunable pulsed dye laser with its output shifted to the ultraviolet region via a nonlinear mixing schemes. One specific example is schematically shown in Fig. 2.10 for generation of the 222 nm photolysis wavelength. The core of this setup is a pulsed dye laser pumped by the second harmonic of a YAG laser at 532 nm. Two stages of frequency doubling and sum frequency generation are used to shift the dye laser output to the ultraviolet region. Specifically, the dye laser output is frequency doubled in the first stage, producing radiation in a near UV region around 282 nm, which is then mixed with the YAG fundamental radiation at 1064 nm in a

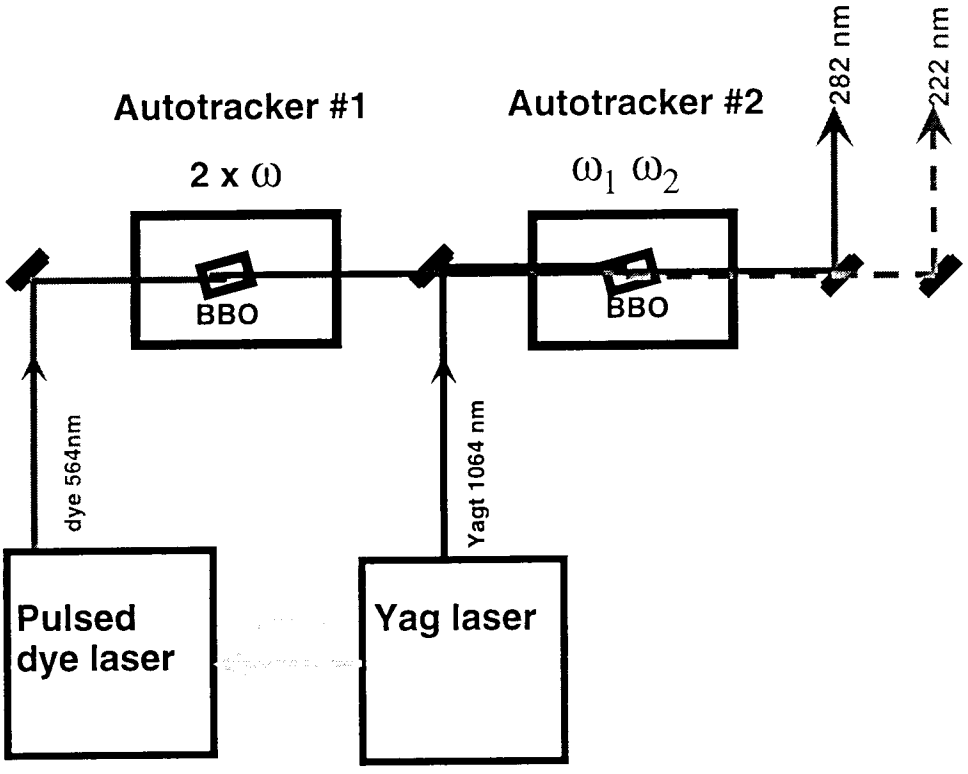

Figure 2.10: Generation of tunable photolysis radiation near 222 nm. Output of the Nd-YAG pumped pulsed dye laser is frequency doubled in first BBO nonlinear crystal and then sum frequency mixed with the Nd-YAG fundamental beam at 1064 nm.

second stage to produce the desired light at 222 nm.

Besides the advantages of tunability, the photolysis beam produced in this way is, unlike the beam from the excimer laser, highly spatially coherent and with minimal astigmatism, which makes precise focusing in the interaction region easier. However the down side is the lower energy of the photolysis pulses and also the higher overall complexity of the setup. Specifically, under typical experimental conditions the dye laser pump efficiency is roughly 23% and therefore 160 mJ/pulse of the dye fundamental radiation is produced with 700 mJ/pulse of the pump radiation at 532 nm. Doubling efficiency in the first nonlinear crystal is typically 20%, yielding 32 mJ of the near UV output. With the excess energy at 1064 nm the second stage yields up to 18% efficiency in conversion of 282 nm input to 222 nm output, and thus about 6 mJ/pulse is finally obtained at the photolysis wavelength, i.e. about factor of 10 less than the energy per pulse typically used from the excimer laser at 248 nm.

2.5 Laser induced fluorescence product detection

2.5.1 Excitation laser requirements

Compared to the high spectral resolution and output energy required for the infrared excitation step, only a fairly modest laser system is needed for probing the OH and OD photoproducts. The three basic requirements of tunability, spectral resolution and output energy for this laser system are briefly considered here. To cover the relevant bands of OH and OD radicals[27,30], tunability over the spectral region 280 nm and 310 nm is needed, which is readily accessible from the frequency doubled pulsed dye lasers operating with rhodamine dyes. The spectral linewidth of

$\Delta\nu \leq 1$ cm^{-1} is sufficient to resolve most of the spectral lines in the OH (OD) excitation spectrum that are important for the OH and OD population analysis. Finally, the energy of the laser should be sufficient to pump approximately 10 % of the OH molecules in the interaction volume to the excited electronic state, i.e. $\sigma_p N_{ph}/S = 0.1$ where σ_p is OH peak absorption cross section, N_{ph} is number of photons per laser pulse and S is the excitation beam cross section in the interaction region. Let us consider a specific example of the $P_1(1)$ line in the $v_{OH} = 0 \leftarrow 0$ sub-band of the $^2\Sigma \leftarrow ^2\Pi$ OH transition. The integrated cross section for this line is 5.0×10^{-16} cm.[31] For Gaussian laser line width of full width at half maximum $\Delta\nu = 1$ cm^{-1} the peak cross section is 4.7×10^{-16} cm^2 and therefore for a beam diameter of 0.1 cm, the required photon output to reach the 10% pumping level is $N_{ph} + 2.5 \times 10^{12}$ photon/pulse, or roughly 2 μJ/pulse at $\lambda = 300$ nm. Over the course of the experiments described in this thesis we used three different laser systems, i) the almost legendary Spectra Physics PDL 2, ii) new and shining Continuum ND-6000, and finally iii) a home-made oscillator-only dye laser with grazing incidence a grating configuration. Indeed, even this final, very simple laser with typical output energies of 2 mJ and 50 μJ in the dye fundamental and second harmonics, respectively, serves quite satisfactorly for purposes of probing OH radical via LIF.

2.5.2 Collection assembly

The collection assembly is a set of mirrors and lenses designed to direct as much of the fluoresecence light as possible to the sensitive area of the detector and at the same time prevent any background scattered light from reaching the detector. Essentially, it

is a high numerical aperture imaging optics that projects the image of the fluorescence excitation region to the detector active area. In the slit jet arrangement the fluorescence is excited along the slit, which provides potentially significant path length advantage compared to a pinhole expansion, provided that the fluorescence is efficiently collected along the whole length of the slit. Two different collection assembly setups have been used in the course of the experimental work; their respective advantages and limitations are briefly discussed below.

The first design shown in Fig 2.11a is essentially the cylindrical analog of the spherical design optimized for pinhole expansions by Majewski *at. al.*[32] Front and rear UV enhanced aluminum coated cylindrical mirrors (5.2 cm radius of curvature) image the cylindrical section at the crossing of the jet and laser beams to a slit of dimensions 0.1×6 cm in the rear mirror, which acts as a spatial filter for rejection of scattered photons that do not originate in the interaction region. Fluorescence that passes through the slit is collected by condenser assembly formed by spherical and cylindrical lenses and is focused on the photomultiplier photocathode.

With the chamber pressure below 10^{-5} Torr, the measured ratio of scattered photons detected by the PMT to the total number per pulse is less than 10^{-9}. The detection efficiency is determined in a Rayleigh scattering experiment using a known pressure of Ar gas in the chamber, from which the fraction collected is estimated to be about 5% over the 4 cm slit length. This is about a factor of 2x lower than expected by geometric considerations, but as much as an order of magnitude larger than for conventional point source imaging.

For optimum performance of this collection assembly, the laser beams need to be

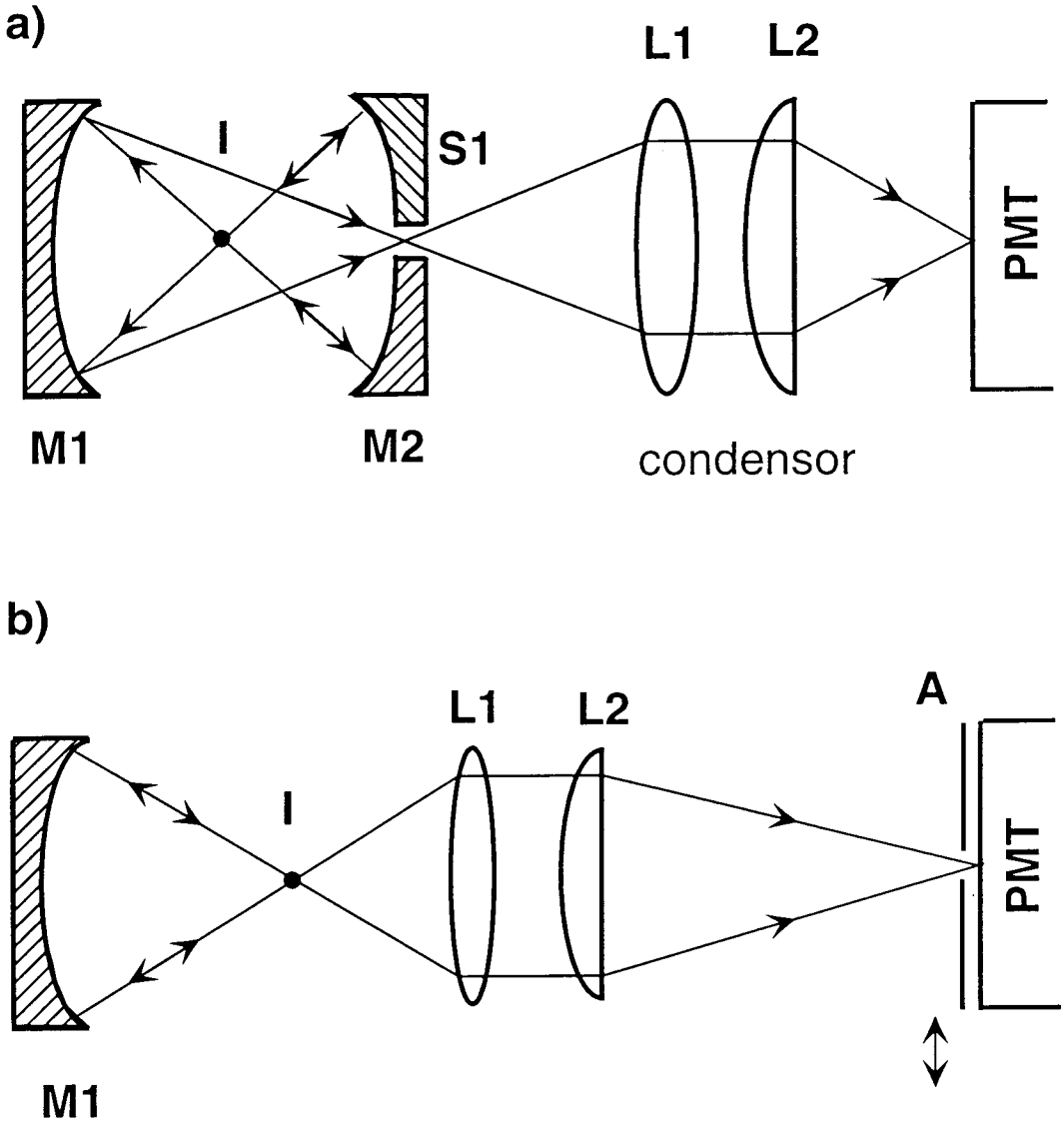

Figure 2.11: The collection assemblies for fluorescence detection is slit geometry LIF detection. The figures represent cuts in the two planes perpendicular to the excitation beam direction.

positioned correctly with respect to the collection mirrors. Indeed, displacement as small as 1 mm results in almost complete loss of the fluorescence signal. This puts rather stringent requirements on alignment of the beams to the vacuum chamber. For the sake of simplicity and ease of use we have also designed and used the simplified collection assembly shown in Fig. 2.11b. Here the back mirror plays the role of the retro-reflector (i. e. increasing the solid angle of detection by a factor of 2). The fluorescence is then collected using the lens condenser. An image of the interaction volume is formed in the plane just in front of the PMT. Aperture (A) placed in this plane plays the role of spatial filter. There is however one important difference compared to the previously discussed collection assemblies. In this simplified design the aperture is placed just in front of the PMT, i. e. outside the vacuum chamber and therefore, its position and shape can be relatively easily changed. Moving the aperture up and down effectively moves the position of interaction volume, from which the fluorescence is collected. Similarly, changing the height and width of this aperture alters the amount of the spatial filtering. Dependence of the signal and/or scattered light on the amount of spatial filtering can therefore be easily tested, which is not straightforward with the original design. While the geometric collection efficiency is somewhat lower for this simplified design, we find the observed fluorescence signals only marginally lower than in the previous case.

A 5 cm square filter assembly in front of the PMT houses filters that reduce the laser scattered light level on the PMT. Usually two dielectric coated notch filters are used, each having greater than 99% reflectivity at the photolysis wavelength. Those notch filters reflect stray photolysis laser light and thus help eliminate problems

typically encountered from bulk absorption filters with fluorescence emitted at longer wavelength. Color glass filters are typically used in series with the reflective filters. Most useful proved to be Schott Glass bandpass filter UG 11 with transmission maximum near 300 nm.

2.5.3 Fluorescence detection

The fluorescence gathered with the collection optics is detected by a photomultiplier (PMT). A PMT detects light at the photocathode which emits photoelectrons by the photoelectric effect. These photoelectrons are electrostatically accelerated and focused on the first dynode of the electron multiplier chain. On impact, each electron liberates a number of secondary electrons which are, in turn, accelerated and focused onto the next dynode. The process is repeated at each subsequent dynode and the electrons from the last dynode are collected at the anode. The PMT used throughout this work is from Electron Tubes Inc. model 9813QB, with 14-dyodes in a linear focus arrangement, which exhibits large gain, fast transient time, and exceptional linearity. The bialkali photocathode and quartz input window provide blue-sensitive response down to 200 nm. Specifications for this PMT provided by manufacturer are listed in Table 2.2.

There are two basic operational modes in which a PMT can operate, i) photon counting and ii) analog measurement modes. Both of those modes will be considered below from the point of view of achievable signal/noise ratio and dynamic range of the detectable signal. The goal of this discussion is to determine the optimum

Table 2.2: Characteristics of the 9813QB PMT

Nominal gain (@ 2060 V)	71×10^6
Maximum cathode-anode voltage (V)	2500
Dark current(Ω^{-1})	500
Risetime (ns)	2.2
Peak quantum efficiency (%)	26

detection in present experiments, i.e. for fluorescence signals with a decay time of about 1 μs following a short excitation pulse, and to identify contributing sources of noise and discuss their relative importance. For each case we will consider off-line noise, i.e. the noise observed on the detector when there is no fluorescence signal present (see Fig. 2.12) and the on-line noise which is observed when the fluorescence signal is present.

The photon counting detection scheme is based on the ability of a PMT to generate observable current pulses that correspond to single detected photons. Those single-photon pulses are detected with a discriminator/counter electronics and their frequency is proportional to the light intensity impinging on the PMT photocathode. The off-line noise is in principle limited by the PMT dark counts, which are specified to be 500 counts·s^{-1} or 5×10^{-4} counts in the 1 μs detection window. The on-line noise is primarily determined by the statistical deviations in the number of photons observed within the detection window. For the average number of detected photons N_s, this deviation is $\sqrt{N_s}$, determined by Poisson statistics. Therefore, the

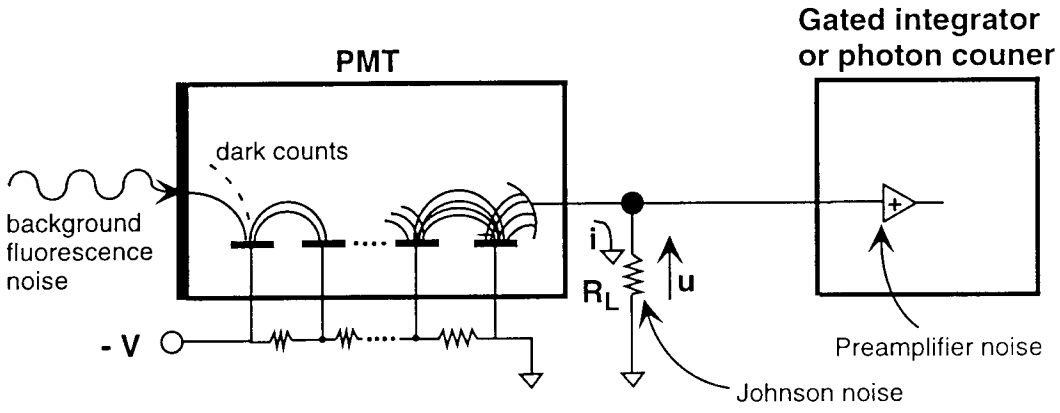

Figure 2.12: Contributions to photomultiplier off-line noise.

signal/noise ratio is

$$\frac{S}{N} = \frac{N_s}{\sqrt{N_s}} = \sqrt{N_s} \,. \qquad (2.3)$$

The major advantage of the photon counting detection is that the off-line noise is very low, limited by the dark count of the PMT, since any analog sources of noise such as preamplifier noise, are very efficiently suppressed by the discriminator electronics. If the signals are averaged over large numbers of pulses, weak signals (with N_s much less than 1) can be readily detected. However the dynamic range of photon counting detection is limited by the counter saturation. Specifically, there is a minimum delay between two detectable single photon pulses, determined by the frequency bandwidth of the photon-counting electronics. Typically this minimum delay is on the order of 5 ns. Therefore, in a 1μs detection window a maximum of 200 photons could be detected, provided they would be regularly spaced. More realistically random photon distribution must be taken into account. If K_s is the average photon flux (in #/second) than the observed signal count is $N_S = K_S \cdot T \cdot e^{-K_S \cdot t}$, where T is the detection gate width and t is the time resolution of the photon counter. For example, for T = 1 μs, t = 5 ns, and the average photon flux of 100 photons in the 1μs window K_s = 100/1,000 ns = 0.1 ns^{-1}. Therefore $N_s = 10 \,.\, e^{-0.1 \times 5} = 61$. Therefore due to the counter saturation only 60% of the detected photons are counted. In other words, already 40% saturation is observed, which limits the dynamic range obtainable with the photon counting method. This detection scheme is therefore most useful for signals of average photon flux of less than 100 detected photons in the 1 μs detection window.

In the analog detection mode the total anode current I is measured which is proportional to the detected photon flux dN_s/dt by the relation

$$I = \left(\frac{dN_S}{dt} \right) \cdot G \cdot q_e \qquad (2.4)$$

where G is the gain of the PMT dynode chain and q_e is the electron charge. For measuring low duty-cycle pulsed signals, such as the fluorescence decays, usually a gated integrator is used to measure an average voltage across a load resistor R_L, in a specified time interval Δt (gate). This gate is set so that the most intense part of the signal is sampled.

Both photon-statistics and analog sources of noise must be considered in this detection scheme. The most straightforward way to include both those contributions in the signal/noise analysis is to express the observed average voltage in terms of the number of detected photons N_S. From Equation (2.4) it directly follows that a single photon voltage signal V_P is

$$V_P = (G \cdot R_L \cdot q_e) \frac{1}{\Delta t} \qquad (2.5)$$

where T is the gate length. Specifically, for the gate length $\Delta t = 1$ μs, the PMT gain G $= 7.1 \times 10^7$, and the load resistor $R_L = 50\ \Omega$, the single photon signal is $V_p = 35.5$ μV. Note that this single photon signal is inversely proportional to the gate length, and for a constant photon flux the observed signal $V_S = N_S \cdot V_P$ is, as expected, independent of the gate width. This single photon signal is essentially a conversion factor between the observed analog voltage signal V_S and the number of detected photons N_S.

The photon statistics Poisson noise is $\delta N_{Poiss} = \sqrt{N_S}$ and therefore in an ideal case

the corresponding voltage noise is

$$\delta V_{Poiss} = V_P \cdot \left(\frac{V_S}{V_P}\right)^{\frac{1}{2}} = \left(V_P \cdot V_S\right)^{\frac{1}{2}} . \qquad (2.6)$$

However, due to the spread in the observed single-photon-pulse intensities, the realistically obtainable Poisson-limited signal/noise ratio is

$$\frac{S}{N} = 0.8\left(\frac{V_S}{V_P}\right)^{\frac{1}{2}} . \qquad (2.7)$$

The two major contributions to the analog noise are i) Johnson noise in the load resistor R_L and ii) preamplifier noise on the input to the gated integrator. The Johnson noise at room temperature is $V_{RMS}/\sqrt{Hz} = (4kTR_L)^{1/2}$. For a 50 Ω load resistor this translates into 0.9 $nV/\sqrt{Hz}$. The preamplifier noise is 2.2 $nV/\sqrt{Hz}$. When those contributions are added in quadrature, the resulting analog off-line noise is 2.4 $nV/\sqrt{Hz}$, which yields to 2.4 μV RMS noise for a 1μs detection gate width. This is more than an order of magnitude less than the signal resulting from a single photon detected in the integration gate U_p = 35 μV. Therefore for signals down to one photon per gate, the on-line noise is limited by the Poisson rather than the analog noise contributions. While the obtainable on-line S/N ratio is only 80% of the photon-counting limit, the advantage of this detection scheme is that the dynamic range is not limited by photon counter saturation.

A final source of noise that has not been discussed is the contribution from the laser scattered light and/or from background fluorescence generated by the laser pulses. The strong photolysis and probe laser pulses that pass through the vacuum

chamber are scattered by the vacuum impurities and by the optical elements in the beam path, such as windows and irises and cause scattered light signals observed by the PMT. It is possible to efficiently discriminate against the Rayleigh scattered light with the proper setting of the signal integration gate and by use of reflective and absorptive filters in front of the PMT that spectrally discriminate against the excitation laser pulses. However, the broadband fluorescence from the vacuum impurities and/or generated in the absorptive filters can not be completely eliminated by either method. Typical contributions from those mechanisms in the present experiments are on the order of 1 photon per gate and thus they in fact represent the limiting source of off-line noise.

Under these conditions, the analog detection scheme provides definite advantages over the photon counting detection and is therefore used for all the experiments described in this thesis. The lack of signal saturation due to the limitations in the counting electronics leads to significantly better over all S/N ratio for the stronger signals, such as from the H_2O and HOD monomer photodissociation. For weak signals, such as from photodissociation of the weakly bound complexes, the overall sensitivity is close to 1 signal photon per pulse, limited mostly by the background fluorescence, not by the analog detection noise contributions.

2.6 Vacuum system

In this section we summarize the design considerations for the vacuum chamber and pumping system that is used for the vibrational mediated photodissociation

experiments in slit supersonic jets. As discussed in previous sections, the use of a slit supersonic expansion, rather than a pinhole, enhances significantly the observed LIF signs, which is an important factor in the success of the present experiments. The price to be paid for this advantage is the high gas throughput for a slit jet compared to typical pinhole jets. Specifically, for the jet dimensions used in our experiments, 40 mm × 50 μm, the limiting orfice area is 2 mm^2, more than 10^2 larger then for a typical pinhole jet (with diameter ϕ = 100 μm). As discussed below, even with the low duty-cycle pulsed valve operation, the gas load is considerable. Moreover, the LIF detection puts more stringent requirements on the background pressure than, for example, direct absorption experiments in the slit jet. Specifically, for direct absorption experiments, background pressures of roughly100 mTorr can be tolerated without compromising the signal/noise ratio. In contrast, broadband fluorescence signals from impurities excited by the UV photolysis and probe laser pulses are readily observed with LIF detection, which under our experimental conditions becomes the dominant source of noise at chamber pressures above 10^{-4} Torr.

2.6.1 Pumping speed considerations

The gas load on the vacuum pumps is determined by the fluid dynamics of the slit expansion. Therefore, a brief overview of the most important results relevant to the present discussion are first presented, with more detailed discussion on the subject found elsewhere.[33,34] The slit jet throughput (σ)depends on the limiting area of the orfice, stagnation pressure, and the nature of the expanding gas and can be expressed as

$$\sigma = P \cdot A \cdot v, \tag{2.8}$$

where A is the area of the jet and P and v are the pressure and velocity at the jet throat. For an atomic gas, these values are related to the stagnation pressure (P_0), temperature (T_0), and mass (M) of the expanding gas by the relations:

$$P = P_0\left(\frac{2}{\gamma+1}\right)^{\frac{\gamma}{\gamma-1}} = 0.487 \cdot P_0 \tag{2.9}$$

$$v = \left(\frac{5 \cdot R \cdot T_0}{4 \cdot M}\right)^{\frac{1}{2}} \tag{2.10}$$

The average throughput for the pulsed slit jet expansion is obtained by multiplying the continuous throughput by the duty-cycle $\delta = \tau \cdot f$, where τ is the width of the gas pulse. Table 2.3 summarizes the throughputs (per unit of stagnation pressure) for He, Ne, and Ar buffer gases at room temperature (T_0 = 300 K) in the stagnation region, calculated for a jet area of $A = 2\times10^{-2}$ cm^2 and a duty cycle $\delta = 10^{-2}$.

Table 2.3: Slit jet characteristics for He, Ne, and Ar buffer gases.

buffer gas	orfice velocity ($cm \cdot s^{-1}$)	average throughput (l/s)	Max. Stagnation pressure (Torr)
Ar	$2.79 \cdot 10^4$	$2.72 \cdot 10^{-3}$	1550[a)]
Ne	$3.95 \cdot 10^4$	$3.85 \cdot 10^{-3}$	1090
He	$8.83 \cdot 10^4$	$8.60 \cdot 10^{-3}$	488

a) for a pumping speed of 4200 l/s and a maximum base pressure of $1 \cdot 10^{-3}$ Torr.

The maximum stagnation pressures in the last column in the Table 2.3 indicate the

maximum stagnation pressure behind the pulsed valve for a given buffer gas, assuming the vacuum chamber is evacuated by a 10" diffusion pump with pumping speed 4200 l/s and maximum inlet pressure of 10^{-3} Torr. However, in practice it is observed that this maximum inlet pressure is somewhat lower because of the pulsed nature of the gas load. For example, for the Ne buffer gas we observe that the diffusion pump starts to "choke" at a stagnation pressure 800 Torr, rather than the predicted 1100 Torr, and the average diffusion pump inlet pressure is $7 \cdot 10^{-4}$ Torr, lower than expected for a diffusion pump. Indeed, under these experimental conditions a single 500 μsec gas pulse with a peak throughput of 308 Torr·l/s delivers 0.15 Torr·l of gas into the vacuum chamber. This temporarily increases the pressure in the 100 liter chamber volume to $1.5 \cdot 10^{-3}$ Torr, which is pushing the limiting inlet pressure for an oil diffusion pump.

2.6.2 chamber design

The overall layout of the vacuum chamber and vacuum pumps assembly is schematically shown in the Fig 2.13. The vacuum chamber is formed by a welded stainless-steel cage-like frame with o-ring sealed aluminum flanges mounted on all six faces, forming a vacuum tight compartment with inside flange-to-flange dimension of 18". Such a design provides easy access to the chamber interior by removing one of the flanges and a high level of flexibility for different applications: It is easy to remove any of the side and/or top flanges and replace it with another flange of same overall dimensions but with different ports mounted to it. For example, in the present application the fluorescence collection optics and the PMT are mounted

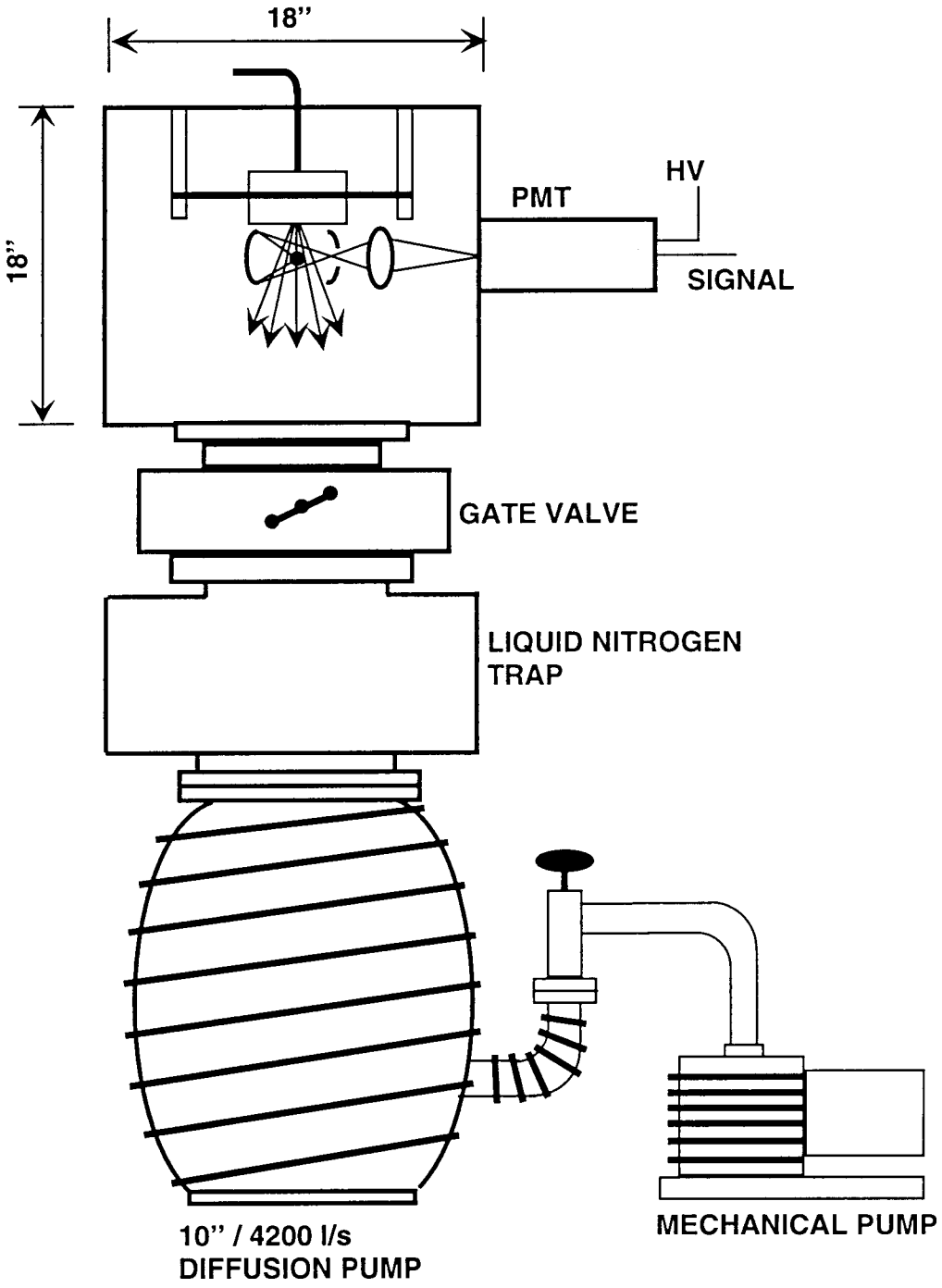

Figure 2.13: Vacuum chamber and pumping system.

directly to one of the side flanges. If desired, this whole flange can be removed and replaced by an ion-detection assembly with a time-of-flight mass spectrometer for REMPI detection scheme. Similarly, the slit pulsed valve assembly mounted to the top flange can be replaced by, for example, a pinhole pulsed valve setup. Thus the same vacuum chamber can be quickly modified for specific applications.

The vacuum chamber is pumped by a 10" (Varian VHS10) diffusion pump with a liquid-nitrogen cooled trap and a gate valve placed between the pump and the chamber in a standard 'tower' configuration.[28] The diffusion pump is backed by a two stage mechanical pump (Edwards M2-80). The base pressure in the chamber is typically $1x10^{-6}$ Torr, limited by degassing from the large aluminum flanges and by the large o-rings that seal the flanges to the basic cage.

2.6.3 Gas handling and mixing manifold

The purpose of gas the handling manifold is to prepare a gas mixture of well controlled composition and deliver it to the pulsed valve at a desired stagnation pressure and/or flow rate. Two basic arrangements have been used in our experiments. In the first arrangement, the gas mixture is prepared beforehand in a large mixing tank so that the composition is determined by partial pressures of individual components. In the second arrangement, the individual components are delivered to the pulsed valve through separate lines and the mixture composition determined by controlling flow in each line with an needle valve.

The setup of the simple gas handling manifold with the mixing tank is schematically shown in Fig 2.14a. A mixing tank of approximate volume 25 liters is

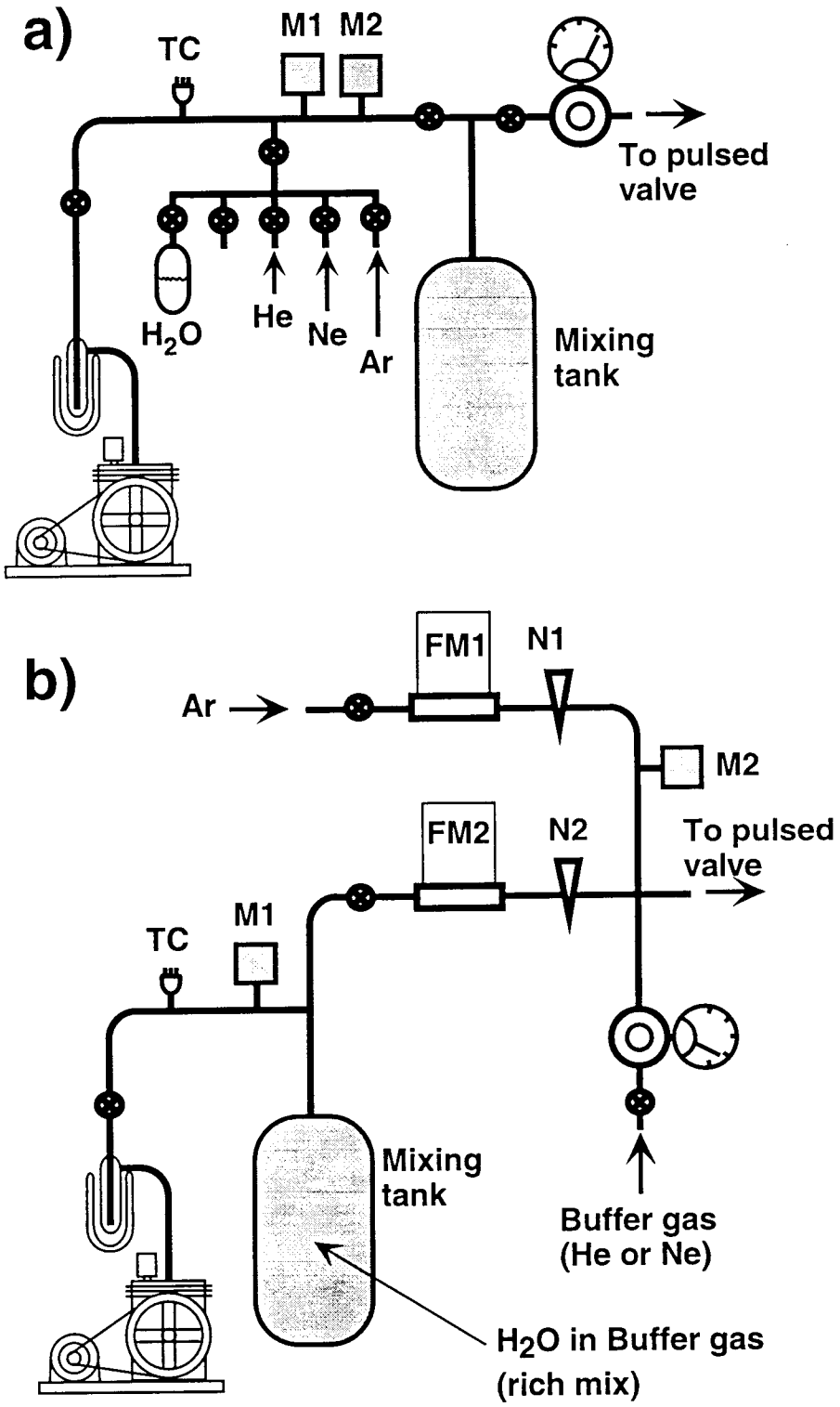

Figure 2.14: Gas handling and mixing manifolds

connected to a gas delivery valve manifold with 5 individual inlet ports and to the input of a pressure regulator that establishes the stagnation pressure for the pulsed valve. Two capacitance manometers M1 and M2 are used to determine the gas mix constituents partial pressures, with 100 and 5000 Torr full ranges, respectively. A thermocouple vacuum gauge TC is used primarily for leak testing purposes. A mechanical pump is used for evacuation of the manifold and the mixing tank and is isolated from the manifold with a liquid N_2 cooled trap to prevent contamination by pump oil. The main advantage of this setup is its simplicity both in construction and operation. The only practical limitation is that it does not provide the flexibility to easily change the gas mix composition while monitoring signals, and therefore optimizing the gas mix can be tedious.

A typical gas mixture contain 0.5 - 1% of H_2O vapor in He buffer gas for the H_2O monomer studies, while 1% H_2O and 30% Ar in Ne buffer gas is the most successful composition for producing the Ar-water complexes in the jet. The mix preparation is started with pumping out the mixing tank to below 100 mTorr. A liquid sample of deionized water is typically purified by three freeze-pump-thaw cycles and then allowed to evaporate into the evacuated mixing tank, monitoring the pressure with a 100 Torr capacitance manometer. No more than 15 Torr of water vapor is used to ensure that liquid water is not formed by condensation inside the gas lines and/or in the pulsed valve. Next Ar gas is introduced to the tank, if required, and finally the buffer gas is added. The total pressure in the tank can be varied between 1500 and 3000 Torr for 1% and 0.5% H_2O fractional concentrations, respectively. Figure 2.14b shows the more sophisticated gas delivery system with flow control. This system

allows for independently changing of the fractional concentrations of two constituents in the gas mix A and B, by controlling their relative flows. Two thermal flowmeters with full range of 400 Torr·l·s^{-1} and 1.6 Torr·l·s^{-1} are used for the major and minor mix constituents, respectively. They are connected in series with two needle valves used to control the gas flow in each of the delivery branches. The third branch connected in parallel to the two flow-control lines is equipped with a pressure regulator and is in some cases used to deliver additional buffer gas to maintain a preset total stagnation pressure. This setup provides much more flexibility, but at the same time requires much more attention and therefore is best suited for gas mix optimization on-the-fly.

References to chapter 2:

1 D. F. Plusquellic, O. Votava, and D. J. Nesbitt, *J. Chem. Phys.* **107,** 6123 (1997).

2 A. Yariv, *Optical Electronic* (Oxford University Press, New York, Oxford, 1991).

3 V. G. Dmitriev, G. G. Gurzadyan, and D. N. Nikogosyan, *Handbook of Nonlinear Optical Crystals* (Springer- Verlag, Berlin, Heidelberg, 1997).

4 A. Fix, T. Schroeder, J. Nolting, and R. Wallenstein, *Applied Laser Spectroscopy* (Plenum Press, New York, 1990).

5 D. E. Withers, G. Robertson, A. J. Henderson, Y. Tang, Y. Cui, W. Sibbett, B. D. Sincleir, and M. H. Dunn, *J. Opt. Soc. Am.* **B,** 1737 (1993).

6 W. R. Bosenberg, L. K. Cheng, and C. L. Tang, *Appl. Phys. Lett.* **54,** 13 (1989).

7 W. R. Bosenberg, W. S. Pelouch, and C. L. Tang, *Appl. Phys. Lett.* **54,** 1952 (1989).

8 Y. X. Fan, R. C. Eckardt, R. L. Byer, C. Chen, and A. D. Jiang, *IEEE J. Quant. Electr.* **25,** 1196 (1989).

9 Y. Tang, Y. Cui, and M. H. Dunn, *Opt. Lett.* , 192 (1992).

10 W. R. Bosenberg and D. R. Guyer, *Appl. Phys. Lett.* **61,** 387 (1992).

11 S. J. Brosnan and R. L. Byer, *IEEE J. Quant. Electr.* **QE-15,** 415 (1979).

12 L. K. Cheng, W. R. Bosenberg, and C. L. Tang, *Appl. Phys. Lett.* **53,** 175 (1988).

13 D. Michael, W., K. Kolenbrander, and J. M. Lisy, *Rev. Sci. Instrum.* **57,** 1210 (1986).

[14] T. K. Minton, S. A. Ried, H. L. Kim, and J. D. McDonald, *Opt. Comm.* **69,** 289 (1989).

[15] E. R. Bosenberg, W. S. Pelouch, and C. L. Tang, *Appl. Phys. Lett.* **55,** 1952 (1989).

[16] D. F. Plusquellic, O. Votava, and D. J. Nesbitt, *Appl. Opt.* **35,** 1464 (1996).

[17] K. K. Lehmann, D. C. Hovde, J. H. Timmermans, and G. Scoles, *Opt. Comm.* **86,** 294 (1991).

[18] C. E. Hamilton and W. R. Bosenberg, *OSA Technical Digest Series* **12,** 370 (1992).

[19] M. J. T. Milton, T. D. Gardiner, G. Chourdakis, and P. T. Woods, *Opt. Lett.* **19,** 281 (1994).

[20] T. W. Hansch and B. Couuillaud, *Opt. Comm.* **35,** 441 (1980).

[21] J. C. Diels and W. Rudolph, *Ultrashort Laser, Pulse Phenomena* (Academia Press, 1995).

[22] E. Riedle, S. H. Ashworth, J. T. Farrell Jr., and D. J. Nesbitt, *Rev. Sci. Instrum.* **65,** 42 (1996).

[23] T. D. Raymond, W. J. Alford, A. V. Smith, and M. S. Bowers, *Opt. Lett.* **19,** 1520 (1994).

[24] D. Hausler, P. Andersen, and R. Schinke, *J. Chem. Phys.* **87,** 3949 (1987).

[25] V. Engel, V. Staemmler, R. L. Vander Wal, F. F. Crim, R. J. Sension, B. Hudson, P. Andersen, K. Hennig, K. Weide, and R. Schinke, *J. Phys. Chem.* **96,** 3201 (1992).

26 G. E. Hall and M. Wu, *J. Phys. Chem.* **97,** 10911 (1993).

27 G. H. Dieke and H. M. Crosswhite, *J. Quant. Spectrosc. Radiat. Transfer.* **2,** 97 (1962).

28 J. M. Moore, C. C. David, and M. A. Coplan, *Building Scientific Apparatus* (Alan M. Wilde, Redwood City, 1989).

29 *Lambda Physik Lextra 50 instruction manual* (1993).

30 M. A. A. Clyne, J. A. Coxon, and A. R. Woon Fat, *J. Mol. Spec.* **46,** 146 (1973).

31 T. J. McGee and T. J. McIlrath, *J. Quant. Spectrosc. Radiat. Transfer* **32,** 179 (1984).

32 W. A. Majewski, D. F. Plusquellic, and D. W. Pratt, *J. Chem. Phys.* **90,** 1362 (1989).

33 G. Scoles, *Atomic and Molecular Beam Methods, Volume 1* (Oxford University Press, Oxford, 1988).

34 C. M. Lovejoy, Ph.D. thesis, University of Colorado, 1990.